OPTIMIZATION OF HORIZONTAL WELL COMPLETIONS USING AN UNCONVENTIONAL COMPLEX FRACTURE MODEL

by

Bryan Kendall Forbes

A thesis submitted to the faculty of
The University of Utah
in partial fulfillment of the requirements for the degree of

Master of Science

in

Petroleum Engineering

Department of Chemical Engineering

The University of Utah

December 2016

The University of Utah Graduate School

STATEMENT OF THESIS APPROVAL

The thesis of **Bryan Kendall Forbes**

has been approved by the following supervisory committee members:

John McLennan	, Chair	**July 14, 2016** Date Approved
Ian Walton	, Member	**July 14, 2016** Date Approved
Arnis Judzis	, Member	**July 14, 2016** Date Approved

and by **Milind Deo** , Chair/Dean of

the Department/College/School of **Chemical Engineering**

and by David B. Kieda, Dean of The Graduate School.

ABSTRACT

Drilling and completion designs have advanced drastically over the last two decades, leading to improved hydraulic stimulation and well production. However, engineers still encounter difficulties addressing the effects of complex natural fractures during hydraulic fracture propagation. Natural fractures can cause unanticipated stress shadowing effects, complex fluid and proppant transport paths, and interactions with hydraulically induced fractures. Proof of concept simulations in this thesis demonstrate that a combination of commercial discrete fracture network (DFN) simulators can be used to qualitatively and quantitatively evaluate stage and cluster placement and improve well design in typical naturally fractured plays. This was possible by 1) analyzing well logging data to develop a discrete fracture network model, 2) simulating fracture network variations resulting from specific design conditions using DFN software packages in tandem, and 3) verifying stimulation and completion design by matching pressure treatment history and evaluating production data acquired from test wells.

Three horizontal test wells were used to analyze the effects of different stimulation and completion strategies on accessing pre-existing natural fractures. Formation microimager (FMI) data acquired from one of the wells were used to represent conductive natural fractures intersected by each lateral. The control well contained a four cluster 120 shot per foot (spf) design. The new cluster design consisted of 10 clusters and 10 spf per stage. Following hydraulic fracturing, pressure treatment history matching using as-

pumped pumping schedules were used to simulate the effectiveness of various completion and stimulation designs. Simulations for a revised cluster design showed a 15% increase in propped fracture area using the same pump schedule.

Simulations results were verified by comparing production data between the three wells over a three-month period. The cumulative BOE production of the limited entry well was similar to the standard wells, but produced 20% less water. Results suggest the new cluster design in this geologic setting has value. The study performed has (1) served as a benchmark for developing an improved understanding of the effects of cluster design complex natural fracture systems and (2) empirically verified that complex fracture modeling simulations can be used in fracture effectiveness for a proposed well.

TABLE OF CONTENTS

LIST OF FIGURES

LIST OF TABLES

CHAPTER 1

INTRODUCTION

In the hydrocarbon extraction industry, wellbore and completion designs are chosen, based on specific reservoir properties, to optimize drainage and field development [1, 2]. Considerations for horizontal well completion design include proppant size and volume, diverter placement, treatment fluid schedule, number of stages, amount of perforations, and location of clusters of perforations along the stage. Additionally, discrete fracture models have advanced the capabilities of modeling existing complex natural fracture systems surrounding a well [3, 4]. Such design choices have a significant influence on the economics of a well, ranging from initial material costs and time required to complete the well to the expected ultimate recovery. Unfortunately, there are challenges when accounting for the effects of natural fractures during hydraulic fracture stimulation. Natural fractures can cause unanticipated stress shadowing effects, complex fluid and proppant transport paths, and interactions with hydraulically induced fractures that are currently difficult to predict. In order to address these challenges, empirically proven discrete fracture simulator packages are developed to include complex natural fracture systems [5, 6].

1.1 Standard drilling and completions design

New completion standards commonly implement uniformly spaced perforation clusters in each stage along the lateral of a well. This is normally refined using a trial-and-error method. The highest producing well is selected as the best model and becomes a template for future operations. This approach is commonly used when limited data are available to strategically place perforation clusters in a nonuniform optimized pattern. Furthermore, comparing the effectiveness of production data to completion design is difficult owing to the lack of viable analysis tools.

Studies have shown that a limited amount of the perforations in a uniform cluster approach account for the majority of production [7]. Figure 1.1 provides proof of this problem in four horizontal gas wells [8]. Inhibited productivity has been attributed to stress shadowing effects, improper targeting of natural fractures during stimulation, and lateral variability in rock properties in the well [9, 10]. A cluster located in a lower stress zone will take more fluid and invoke fracture initiation because it is the path of least resistance. This behavior is seen in Figure 1.2 by overlaying microseismic events over a minimum stress log [11]. In Figure 1.2, red represents low minimum horizontal stress and blue depicts high horizontal stress. Note that the microseismic color is the same as the simulated stage in each of the four cases. Consequently, fractures are only induced in regions where the perforations are placed in the lowest stress zone. As a result, poor fracture coverage and distributions are generated and leads to underutilized perforations that account for little to no production.

1.2 Limited entry and its success

Another approach that is an improvement over the trial-and-error/uniform geometry method is the so-called engineered method for selection of stages and cluster spacing/geometry. This technique analyzes well logs to determine the optimum location for the clusters of perforations. The number of inefficient perforations is reduced by targeting uniform hydraulic and natural fracture initiation and decreasing treatment pressure [11, 12]. The most common design approach for the engineered method is described by Cipolla et al. (2011). The technique relies on placing perforations in regions of the payzone where rock properties are similar. This is advocated to create the optimum amount of fracture area in a lateral well. Rock properties considered (but not limited to) are the in-situ stresses, Young's modulus, Poisson's ratio, and rock compressibility

The engineered method can be more difficult to use in heterogeneous rock with high variations in stress. Typically, limited entry calculations determine the perforation locations that will generate an equal fluid distribution per perforation. This design approach is possible by fixing the cluster spacing and increasing the number of stages or fixing the stages and varying the cluster spacing. Generally, the number of stages are held constant and the clusters are placed in locations where the rock stresses will be similar. In this scenario, global breakdown occurs, fluid distribution will be even, and thus ultimately leads to an increase in production.

1.3 Stochastic representation of diversion

Substantial variations in the minimum principal stress (which needs to be overcome for fracture propagation) are not uncommon along a lateral. Limited entry designs attempt

to optimize perforation placement to achieve equal fluid distribution. Cluster frequency alone cannot overcome the challenges associated with stress variation and anisotropy.

One of the solutions to overcome stress variability is the implementation of near-wellbore diversion techniques. The goal of diversion is simple: block the perforations with the currently preferred fluid path and redirect flow. However, certain pumping and material design choices must be considered for diversion optimization. A material must be large enough and shaped properly to isolate the perforation over a specific time to properly divert a well. Typical commercial diverting agents consist of ball sealers, benzoic acid flakes, gilsonite, rock salt, wax beads, and various other water soluble and oil soluble products. Table 1.1 provides some design considerations when selecting a diverting agent [13].

Incorporating commercial diverting agents into completion designs has shown varying success. The effectiveness of diverter materials on multistage horizontal wells have been a particular area of interest [13]. However, empirically validated evidence on the efficiency of diverting agents based on horizontal well production is still limited. This problem is further confirmed by Allison et al. (2011) who proposed a need for further study [14].

1.4 Purpose of using an unconventional fracture model

Microseismic events have shown that complex hydraulic network profiles in shale and carbonate formations are common occurrences [15, 16, 17]. This behavior invalidates the feasibility of using a bi-wing hydraulic fracture simulator for modeling unconventional reservoirs. Wire mesh models have been developed to counter challenges associated with natural fractures [17, 18]. A rudimentary wire mesh simulator includes two orthogonal sets

of parallel and uniformly spaced sets to account for the natural fractures. They are able to account for the general storage area, surface area, and interactions with the hydraulic fracture network. However, the model is unable to properly account for proppant placement and perform accurate posttreatment analysis. Furthermore, the symmetrical natural fracture sets are not accurate representations of the natural fracture network along the wellbore. These limitations suggest a need for a more rigorous hydraulic fracture simulator.

Schlumberger has observed similar problems with available fracture software packages. An unconventional fracture model (UFM) has been developed and integrated into Mangrove, a Petrel add-on [19]. The UFM is capable of simulating propagation, deformation, and fluid flow in hydraulic and natural fractures. Also, postfracture reports allow the user to evaluate the effect of cluster spacing and diversion based on how much fracture area was generated due to hydraulic and natural fractures.

Mangrove is considered a leading industry fracture modeling tool. It was used for the majority of simulations in this study. However, it contains user limitations when manipulating and generating natural fracture sets specific to a well. Also, for the purposes of this study, diverter is accounted for by stopping a simulation at specific points in a pump schedule, identifying the fractures where the majority of diverter exists, exporting the fracture set and eliminating the fractures holding the majority of proppant, re-fracking the data set, and analyzing new diverter and fracture paths. The final surface area and the surface area of the eliminated fractures are accounted for at the end of the simulation. A software package capable of aiding Mangrove in the mentioned process is FracMan, a discrete fracture network (DFN) modeling package developed by Golder Associates Inc.

Both FracMan and Mangrove are commonly preferred industry choices for fracture

analysis. Yet, both tools have limitations. Individually, the software suites cannot evaluate the design considerations in this study. Therefore, both packages are used in tandem to build a complex fracture dataset that can be manipulated, simulate fracture propagation using an unconventional fracture model, and progressively re-fracture datasets while stopping the pump schedule at key points to account for the effects of diversion and cluster design.

1.5 Thesis overview

This thesis presents the results of simulations of a number of horizontal multistage well designs in an oil reservoir. The simulations are original in that they used a combination of discrete fracture modeling software packages. The chapters in this thesis are as follows:

- Chapter 2 begins with the theory used in the unconventional fracture model (UFM), accounting for hydraulic and natural fracture interaction, stress shadowing effects, and the governing equations for hydraulic fracture propagation.
- Chapter 3 includes the workflow progress with input parameters pertaining to the wellbore design, stochastic natural fracture set generation and validation, rock properties based on logging and core data, and the pump schedule.
- Chapter 4 presents the UFM simulation results and also compares six-month production data of three nearby horizontal wells with differing completions designs.
- Chapter 5 concludes the thesis project and provides suggestions for future studies.

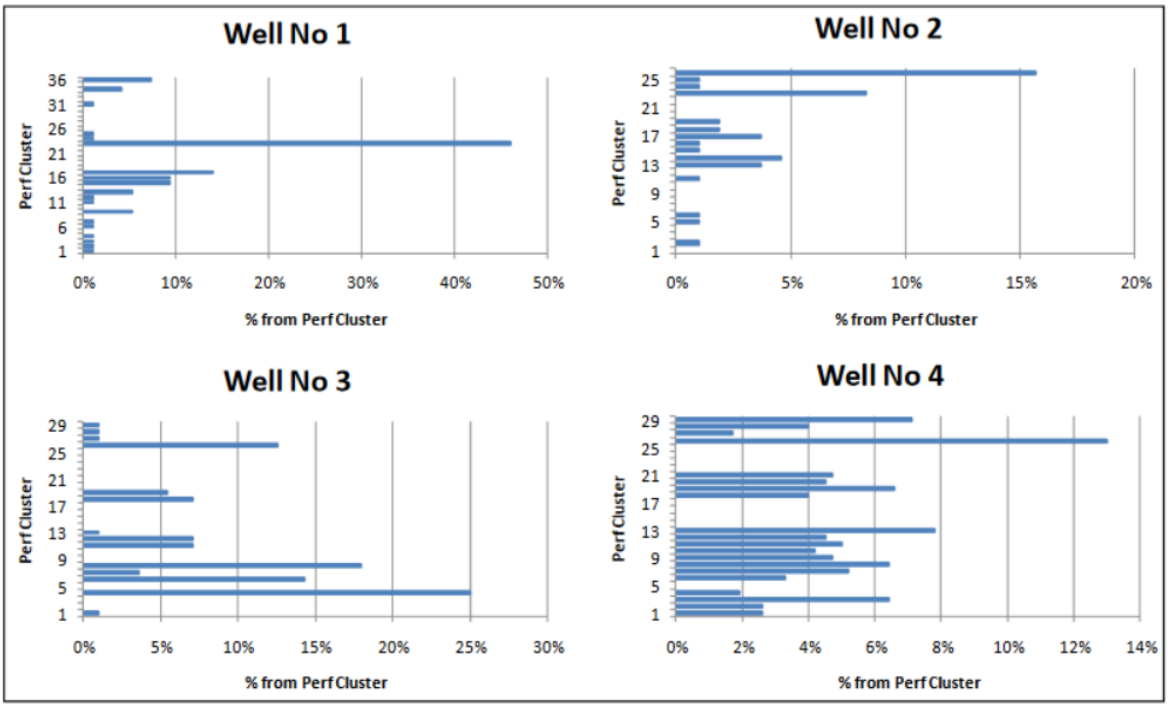

Figure 1.1. Production data of four horizontal gas wells. Results indicate that multiple perforation clusters are producing little to no gas due to poor spacing design.

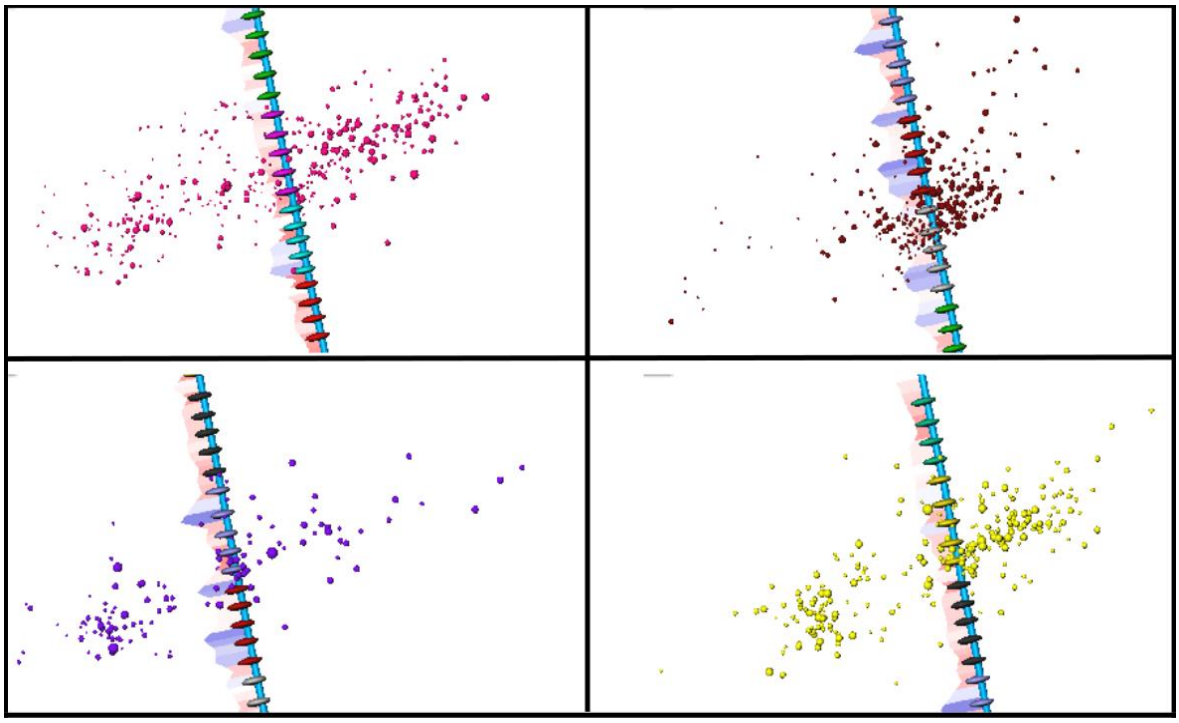

Figure 1.2. Microseismic event overlaying a minimum stress log. Regions of red indicate low stress and blue represents high stress.

Table 1.1: List of common diverting agents and their drawbacks

Diverting Agent	Drawbacks
Ball Sealers	Cannot be used for open hole wells Requires constant pressure for balls to remain seated Inefficient when perforations erode Degradation time must be accurate or efficiency severely drops
Benzoic acid flakes	Very brittle and can break during pumping
Gilsonite	Mesh sizes are typically too high to bridge wellbore widths
Rock Salt	Dissolution rate is highly dependent on formation salinity Requires saturated brine as a pump fluid Requires special surface storage tanks
Wax beads	Applicable only in low temperature wells ($<180^0$ F)

CHAPTER 2

UNCONVENTIONAL FRACTURE MODEL

METHODOLOGY

Satisfying the objectives of this study requires the construction of a geomechanical model using commercial software that can infer the extent of in-situ natural fracturing, comprehend production changes based on cluster perforation design, and assess the effectiveness of diversion in fracture stimulation. No one numerical simulator can currently fulfill these needs without manipulating the model. The model is altered by utilizing the capabilities of two complex fracture simulators in tandem. FracMan — developed by Golder Associates — is used for building and validating the framework of the model. It is one of the more efficient platforms for stochastically representing natural fractures. FracMan's well and natural fracture sets were imported into Mangrove, and populated with the necessary parameters to simulate the effects of a complex natural fracture system.

Mangrove's unconventional fracture model (UFM) simulates fracture stimulation, deformation, fluid flow, and proppant transport within a natural fracture system. The interactions between hydraulic and natural fractures considered by implementing a crossing algorithm developed from experimental work by Renshaw and Pollard [20]. The solutions to fluid flow and elastic deformation are similar to the governing equation of a pseudo-3D discrete fracture model. The major difference of the UFM is solving the

problems with multiple fractures. Figure. 2.1 illustrates the difference between a planar fracture and complex fracture simulation. Accounting for the behavioral effects of natural fractures in the UFM require modifications to existing fracture modeling equations used in traditional simulators and the inclusion of new solutions. The remaining sections in Chapter 2 focus on the new and modified solutions used to construct UFM.

2.1 Governing equations

The governing equations account for the physical processes affecting fracture propagation. This includes fracture deformation mechanics, fluid flow behavior, and fracture propagation criterion. The horizontal wells assessed contain mainly vertical natural fractures (discussed further in the FMI analysis chapters) and are within reason when applied to the UFM. The basic governing equations consist of seven equations listed as follows:

- Fracture power-law fluid flow

$$\frac{\partial p}{\partial s} = -\alpha_0 \frac{1}{\overline{w}^{2n'+1}} \frac{q}{H_{fl}} \left| \frac{q}{H_{fl}} \right|^{n'-1} \tag{2.1}$$

$$\alpha_0 = \frac{2K'}{\phi(n')^{n'}} \left(\frac{4n'+2}{n'} \right)^{n'} ; \; \phi(n') = \frac{1}{H_{fl}} \int_{H_{fl}} \left(\frac{w(z)}{\overline{w}} \right)^{\frac{2n'+1}{n'}} dz$$

The Poiseulle equation determines fluid flow in each fracture element. It is not limited to power-law behavior. Newtonian fluid behavior, slickwater for example, may be considered for the case of n'=K'=1. Fluid characteristics are discussed further in section 3.4.

- p .....Fluid pressure
- q ..... Local flow rate,
- Hfl ..... Height of the fluid in the fracture,
- $\overline{w}$ .....Average width,
- n' ..... Power-law index,
- K ..... Consistency index,
- s..... Distance along the fracture

- Local mass balance

$$\frac{\partial q}{\partial s}+\frac{\partial(H_{fl}\overline{w})}{\partial t}+q_L=0 \tag{2.2}$$

$$\frac{\partial q}{\partial s}+\frac{\partial(H_{fl}\overline{w})}{\partial t}+q_L=0$$

The local mass balance accounts for every fracture. Based on poststimulation reports and diagnostic fracture injection tests (DFIT), the efficiencies were high and the leakoff coefficient was negligible. Sections 3.2 and 3.4 will elaborate more on this observation.

- CL .....Leakoff coefficient,
- hL..... Leakoff zone height,
- τ0(s) .....Time when each fracture element is exposed to fluid

- Global volume balance

$$\int_0^t Q(t)dt=\int_0^{L(t)} H\overline{w}ds+\int_{H_L}\int_0^{L(t)}\int_0^t q_L dtdsdh_l \tag{2.3}$$

- Q(t) ..... Total pump rate,
- L(t) .....Summation of all fracture lengths at time t,
- H(s,t) .....Fracture height at a point in a fracture at time t

- Sum local flow rate

$$\sum_i q_i(t) = Q(t), i = 1,..N_{perf} \tag{2.4}$$

- q(t) ..... Local injection rate into each perforation

- Fracture width

$$w(x, y, z) = w(p(x, y), H, z) \tag{2.5}$$

A 2D plane strain solution for fracture widths is used, and performs similar to a cell-based pseudo-3D model, for the sake of computational efficiency. Vertical and horizontal fracture growth for a pseudo-3D case is considered separately and calculated from a local pressure and vertical stress profile. However, this approach requires fracture initiation and propagation to remain in the lowest stress zone. In this study, some of the cluster perforations of the proposed wells lie in higher stress layers and will eventually break into lower stress regions. This causes inaccurate accounting of fracture height growth and requires a more feasible approach. Consequently, a “Stacked Height Growth” model is integrated into the UFM a discussed further in section 2.2.

- 2D PKN width

$$\overline{w} = \frac{\pi H(p - \sigma_n)}{2E'} \tag{2.6}$$

- E'..... Plane strain Young's modulus

The Perkins-Kern-Nordgren (PKN) model determines the average width in regions of uniform in-situ stresses and a fixed height [21]. Equation 2.5 reduces to 2.6 in these limiting cases.

- Fracture tip boundary conditions

$$p = \sigma_n, W = 0, q = 0 \tag{2.7}$$

The equations presented are solved at each time step to simultaneously determine the fracture opening, localized pressure, and local fluid flow in each fracture element. They will be the underlying basis for providing a stochastic solution for the study.

2.2 Stacked height growth model

The goal of the stacked height growth model is to enhance the pseudo-3D (P3D) model when perforations are located in higher stress zones. The current approach to a P3D model assumes an elliptical bi-wing fracture where the perforation initiates and remains in the lowest stress zone. The bi-wing model is limited and restricted to propagation of a single front.

During simulations, the fluid pressure near the wellbore is assumed higher than the

fracture tip. Eventually, fractures may break through into a lower stress zone and lead to run-away height growth (Figure 2.2). In a real situation, height breakthrough into a lower stress region (Figure. 2.3b) would cause propagation to break into two fracture fronts. As a result, fluid pressure would delineate between the two fracture fronts, contain height growth, and produce different fracture behavior from current pseudo-3D models.

Modifying the P3D model requires new solutions that can account for fracture growth outside the lower stress zones and bifurcation of the fracture fronts on the same vertical plane. Such enhancements require more computational time, but are significantly faster than a planar 3-D simulation. The proposed solution incorporates a cell-based vertically stacked fracture system for multiple P3D fractures on the same plane (Figure 2.3). In the new model, the vertical cells are treated separate from the cells residing from the perforation initiation zone and are placed in a generated proposed initiation zone once breakthrough occurs into a lower stress region. This solution allows for more accurate accounting of vertical flow and height growth during height breakthrough. As stated, the development of an enhanced model requires modifications to the previous P3D model. General solutions will be listed and further details may be referenced from Economides, M.J [22]. The remainder of this section will focus on width and height solutions for multiple fracture propagation sets in a Stacked Height Growth scenario.

- Width calculations

The current P3D model assumes a single fracture front and uses the superposition principle for determining the fracture width (Eq. 2.8). This assumption is reasonable due to the top fracture element being the fracture tip. In the Stacked Height Growth model, the top and bottom fracture elements are not always the fracture tips and can also be contacting

other elements. Therefore, Eq. 2.8 is modified into the form of Eq. 2.9. Detailed solutions of Eq. 2.9 can be referenced in Appendix A.

$$w(z)=\frac{4}{E'}\left[p_{cp}-\sigma_n+\rho_f g(h_{cp}-z)\right]\sqrt{z(h-z)}+\frac{4}{E'\pi}\sum_{i=1}^{n-1}(\sigma_{i+1}-\sigma_i)\left[\begin{array}{l}(h_i-z)\cosh^{-1}\left(\dfrac{z\left(\dfrac{h-2h_i}{h}\right)+h}{|z-h_i|}\right)\\ +\sqrt{z(h-z)}ar\cos\left(\dfrac{h-2h_i}{h}\right)\end{array}\right] \qquad (2.8)$$

$$w(h,z)=\frac{4}{E\pi}\sum_{j=1}^{Nstack}\int_{H_{j-1}}^{H_j}\left|P_{cp,\,j}+\rho_{f,\,j}g(h_{cp,\,j}-a)-\sigma(a)\right|\times\cosh^{-1}\left|\frac{z\left(\dfrac{h-2a}{h}\right)+a}{|\,z-a\,|}\right|da \qquad (2.9)$$

- w(h,y) .....Width profile at given depth and distance from perforation,
- j .....Reference element integer,
- hcp,j ..... Reference depth,
- σ(a) ..... Element in-situ stress,
- Pcp ..... Pressure in the fracture at a reference depth hcp,j,
- ρcp,j ..... Fluid density at a reference depth hcp,j,
- g ..... Gravity,
- h ..... Fracture height,
- H .....Height of the stacked element,
- a ..... Element height as a function of Hj,
- z.....Depth

- Height growth

Height growth is calculated based on the top and bottom intensity factor of a fracture. Eq. 2.10a and 2.10b define intensity solutions in Mangrove.

$$K_{Iup} = \sqrt{\frac{2}{\pi h}}\left[P_{cp} + \rho_f g(h_{cp} - \frac{3}{4}h) - \sigma_n \right] + \sqrt{\frac{2}{\pi h}} \sum_{i=1}^{n-1} (\sigma_{i+!} - \sigma_i) \begin{bmatrix} \frac{h}{2} \arccos\left(\frac{h-2h_i}{h} \right) \\ -\sqrt{h_i(h-h_i)} \end{bmatrix} \qquad (2.10a)$$

$$K_{Iup} = \sqrt{\frac{2}{\pi h}}\left[P_{cp} + \rho_f g(h_{cp} - \frac{h}{4}) - \sigma_n \right] + \sqrt{\frac{2}{\pi h}} \sum_{i=1}^{n-1} (\sigma_{i+!} - \sigma_i) \begin{bmatrix} \frac{h}{2} \arccos\left(\frac{h-2h_i}{h} \right) \\ +\sqrt{h_i(h-h_i)} \end{bmatrix} \qquad (2.10b)$$

Similar to the width equations, the stress intensity factors are calculated based on the local pressure and stress along the entire fracture cross section. The stacked height growth model makes adjustments by calculating the stress intensity for each stacked element in the cross section (Eq 2.11a and 2.11b). Detailed solutions of the new stress intensity equations are listed in Appendix B.

$$K_{Iup} = \sqrt{\frac{2}{\pi h}} \sum_{j=1}^{Nstack} \int_{H_{j-1}}^{H_j} \left| P_{cp,\,j} + \rho_{f,\,j} g(h_{cp,\,j} - a) - \sigma(a) \right| \sqrt{\frac{a}{h-a}} da \qquad (2.11a)$$

$$K_{Idown} = \sqrt{\frac{2}{\pi h}} \sum_{j=1}^{Nstack} \int_{H_{j-1}}^{H_j} \left| P_{cp,\,j} + \rho_{f,\,j} g(h_{cp,\,j} - a) - \sigma(a) \right| \sqrt{\frac{a}{h-a}} da \qquad (2.11b)$$

The stacked height growth equations are an improvement compared to the limitations observed in a P3D model. Fracture prediction is less accurate than a planar 3D model, but requires less computation time and simulates fracture behavior within reason. For this study, the stacked height growth option will be used within Schlumberger's Mangrove software package and predict accurate fracture propagation when perforations are located in higher stress layers.

2.3 Hydraulic and natural fracture interaction

The main draw to using Mangrove's unconventional fracture model is the ability to solve fracture propagation problems related to a complex natural fracture system. Furthermore, the tool accounts for the interactive behavior when a hydraulic fracture approaches a natural fracture. This is an important consideration with the existence of naturally fractured reservoirs.

The behavior between hydraulic and complex fractures is a very complex process and one of the core reasons for the creation of a complex fracture system. A stress field exists at the tip of a hydraulic fracture. Several propagation events may occur based on the magnitude of the stress field and geomechanical properties of existing natural fractures. Figure 2.4 illustrates possible event paths [23]. Three possible propagation cases exist:

1) Fracture tip pressure is not high enough to overcome the minimum in-situ stresses and slips, causing dilation in the natural fracture (2.4d)
2) The hydraulic fracture crosses the natural fracture and remains planar (2.4e)
3) Fluid pressure is high enough for crossing and slippage (2.4f)

Each of the three behaviors may change due to fluid pressure variation during pumping. A

crossing criterion considering the cases listed has been developed by Gu and Weng based of experimental work by Renshaw and Pollard [20, 23]. This criterion considers rock characteristics, rheological properties, leakoff 18ffects, and the angles of interaction.

- Crossing criterion

The natural fractures are considered interfaces when addressing mechanical interactions with hydraulic fractures. The angle of intersection between a hydraulic fracture and natural fracture is β (Figure 2.5). The stress field of the in-situ and shear stresses σ_h, σ_H, and τ_{xy} is defined by the following:

$$\sigma_x = \sigma_H + \frac{K_1}{\sqrt{2\pi r}}\cos\frac{\theta}{2}\left(1-\sin\frac{\theta}{2}\sin\frac{3\theta}{2}\right) \tag{2.12}$$

$$\sigma_y = \sigma_h + \frac{K_1}{\sqrt{2\pi r}}\cos\frac{\theta}{2}\left(1+\sin\frac{\theta}{2}\sin\frac{3\theta}{2}\right)$$

$$\tau_{xy} = \frac{K_1}{\sqrt{2\pi r}}\sin\frac{\theta}{2}\cos\frac{\theta}{2}\sin\frac{3\theta}{2}$$

- K1 ..... Stress intensity factor,
- r ..... Polar length,
- θ ..... Polar angle

Crossing the natural fracture interface requires the maximum principal stress σ_1 to be equal to the rock tensile strength:

$$\sigma_1 = T_0 \tag{2.13}$$

For the case of $\theta = \beta = \beta - \pi$, the maximum principal stress can be determined from Eq. 2.12. For Eq. 2.13 to be satisfied, the fracture interface must not slip, allowing the fracture tip stress field to be transferred across the interface. Jaeger et al. developed interface slippage conditions based on the following [24]:

$$\left|\tau_\beta\right| < S_0 - \mu\sigma_{\beta,y} \tag{2.14}$$

- $\tau\beta$.....Shear stress on the interface,
- $\sigma\beta,y$.....Normal stress on the interface,
- S0 ..... Cohesion of the interface,
- μ ..... Coefficient of friction

Note that Eq. 2.14 also applies to instances when the natural fracture is filled with a weak cementation material.

It is possible to numerically determine whether a fracture will cross or slip when interacting with a natural fracture interface at a given angle β by combining the mentioned equations and the experimental work of Renshaw and Pollard. The original work of Renshaw and Pollard developed an orthogonal crossing solution that is not applicable for all crossing cases. Gu and Weng extended the crossing criteria to nonorthogonal cases by considering local stresses, rock properties, and interface characteristics [25]. Figure 2.6 is an example of the extended crossing results at different angles β for the case of no tensile strength and cohesion of the interface. Essentially, the smaller the angle of intersection, the

more difficult it becomes for crossing to occur. Additionally, the angle of intersection is a very sensitive parameter in determining the crossing criteria.

The extending nonorthogonal criterion presented has been validated by experimental work and quantitatively accounts for whether crossing or slippage will occur [20, 23, 25]. The criterion requires the use of a numerical simulator that accounts for each of the mentioned parameter inputs. Mangrove's UFM implements the crossing behavior defined and accounts for natural fracture effects during hydraulic fracture stimulation.

2.4 Stress shadowing effects

Fracture propagation is highly dependent on the mechanical interactions between nearby hydraulic and natural. Interaction consider nearby fracture stress fields generated by each fracture being displaced due to opening or shearing. For the case of a 3D, plane-strain, displacement discontinuity solution, Olson et al. (2004) improved on the solution provided by Crouch and Starfield describing the normal and shear stresses acting on a fracture element due to opening and shearing of other nearby elements (Eq. 2.15) [26, 27].

$$\sigma_n^i = \sum_{j=1}^{N} G^{ij} C_{ns}^{ij} D_s^j + \sum_{j=1}^{N} G^{ij} C_{nn}^{ij} D_n^j \qquad (2.15)$$

$$\sigma_s^i = \sum_{j=1}^{N} G^{ij} C_{ss}^{ij} D_s^j + \sum_{j=1}^{N} G^{ij} C_{sn}^{ij} D_n^j$$

- C_{ns}^{ij} ..... Normal stress at *i* from a shear displacement discontinuity at *j*,

- C_{nn}^{ij} ..... Normal stress at *i* from an opening displacement discontinuity at *j*,
- C_{sn}^{ij} ..... Shear stress at *i* from an opening displacement discontinuity at *j*,
- C_{ss}^{ij} ..... Shear stress at *i* from a shear displacement discontinuity at *j*

The normal and shear stress (σ_n^i and σ_s^i) acting on the *i*-th fracture element is induced from shear and opening discontinuities (D_n^j and D_s^j) on the *j*-th element. C_{ij} are the 2D, plane-strain elastic influence coefficient at element *i* generating normal stress or shear due to a shear or normal opening displacement discontinuity at element *j*. Lastly, G_{ij} acts as a correction factor that accounts for 3D effects from fracture height that leads to decaying of interaction between two fracture elements when distance increases [19, 27].

The normal stresses of each fracture element due to stress shadowing is computed at each time step in the UFM. The stresses input into the in-situ stress field are placed on each fracture element in the height growth, width, and fracture interaction equations. The summed stresses from stress shadowing effects are very important for the highly natural fractured system in this study.

2.5 Proppant transport

A key process in hydraulic fracturing is the transportation of proppant in a fluid system. The main goal of proppant is to lessen fracture closure once pressure drops. Proper accounting for the parameters that effect proppant travel is significant for reliable simulation of hydraulic fractures. The parameters considered in the UFM are leakoff, bridging, packing, settling, bank erosion, and convective transport [19]. Computational speed is improved upon by assuming a 1D horizontal transport model. Vertical positioning

of the proppant bank, slurry, and clean fluid are computed in each fracture element.

The numerical implementation of fluid and proppant transport in the UFM determines the material locations within each fracture element at explicit time steps. Proppant transport are determined from volumetric concentration of the fluid and proppant components averaged over the element volume above the proppant bank (Eq. 2.16)

$$c_k = \frac{1}{\Delta x' \overline{w}(H - H_{bank})} \int_{H_{bank}}^{H} \int_{-\frac{\overline{w}}{2}}^{\frac{\overline{w}}{2}} \int_{x_c' - \frac{\Delta x'}{2}}^{x_c' + \frac{\Delta x'}{2}} X_k(x', y', z)\, dx'\, dy'\, dz \qquad (2.16)$$

- Xk .....Volume fraction of fluid or proppant identified by index k,
- Δx' .....The length of the fracture element,
- xc.....Fracture element reference length,
- H ..... Height of the fracture element,
- Hbank..... Height of the proppant bank,
- ck..... Concentration of the fluid of proppant identified by index k,
- $\overline{w}$ .....Average width of the fracture element

Being able to account for the volumetric concentration proppant within each fracture element is essential. Diverter will be simulated as "proppant" and be used to determine the fractures containing the majority of proppant during certain stages of a pump schedule. The process of modeling diversion will be elaborated on more in section 3.4.

The settling velocity for solids is determined by the Stoke's law solution for power law fluids presented by Daneshy [24]:

$$v_{set,k} = \left[\frac{1}{3^{\bar{n}'-1}18} \frac{\left(\rho_{prop,k} \bar{\rho}_{fl}\right)}{\bar{K}'} g D_k^{\bar{n}'+1} \right]^{\frac{1}{\bar{n}'}} \quad (2.17)$$

- vset,k ..... Settling velocity for proppant index k,
- $\bar{n}'$ .....Averaged flow behavior index,
- $\bar{K}'$ ..... Averaged flow consistency index,
- g ..... Gravity,
- ρprop,k ..... Proppant density identified by index k,
- Dk .....Proppant diameter identified by index k
- $\bar{\rho}_{fl}$ ..... Settling velocity for proppant index k

Multiple proppant materials are available in Mangrove's database. Also, custom fluid and proppant types can be added if the K', n', diameter, and density values are known

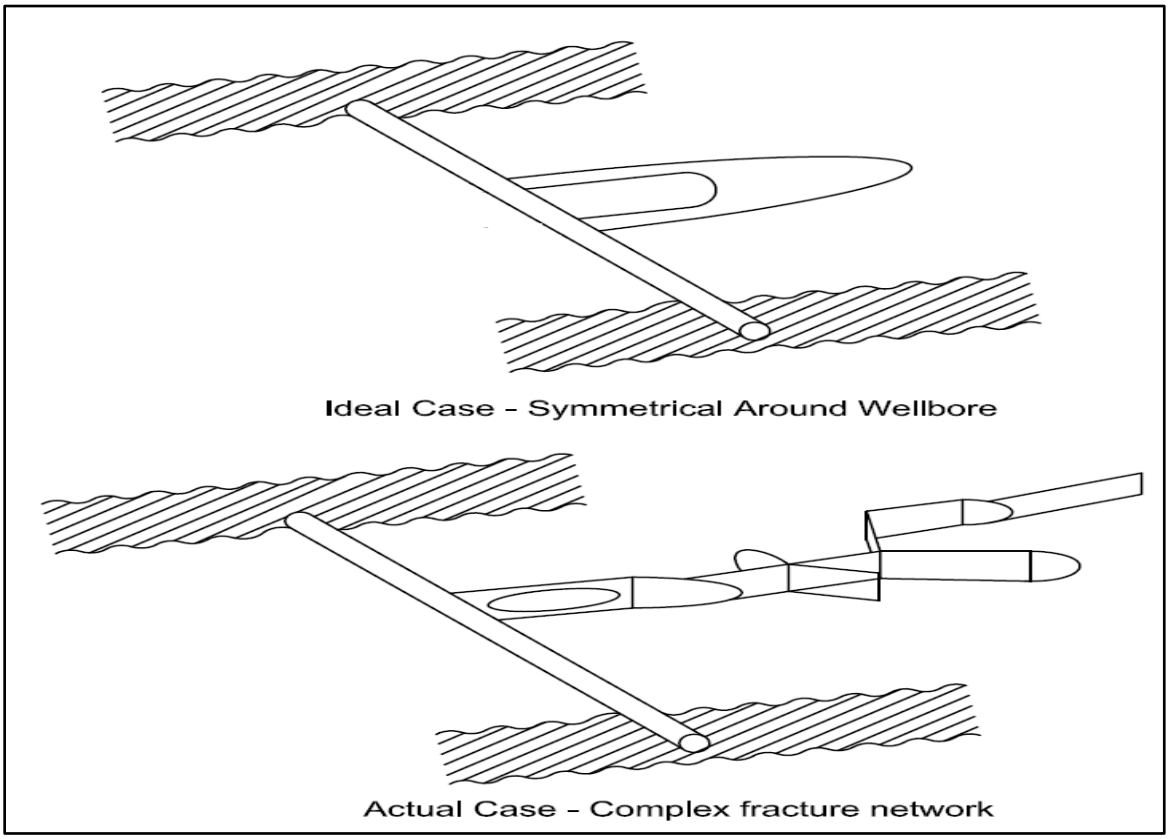

Figure 2.1. Ideal versus actual hydraulic fracture behavior. Multiple industry used hydraulic fracture simulators only consider an ideal planar hydraulic fracture. Complex fracture software packages are able to account for more accurate interactive effects between hydraulic and natural fractures.

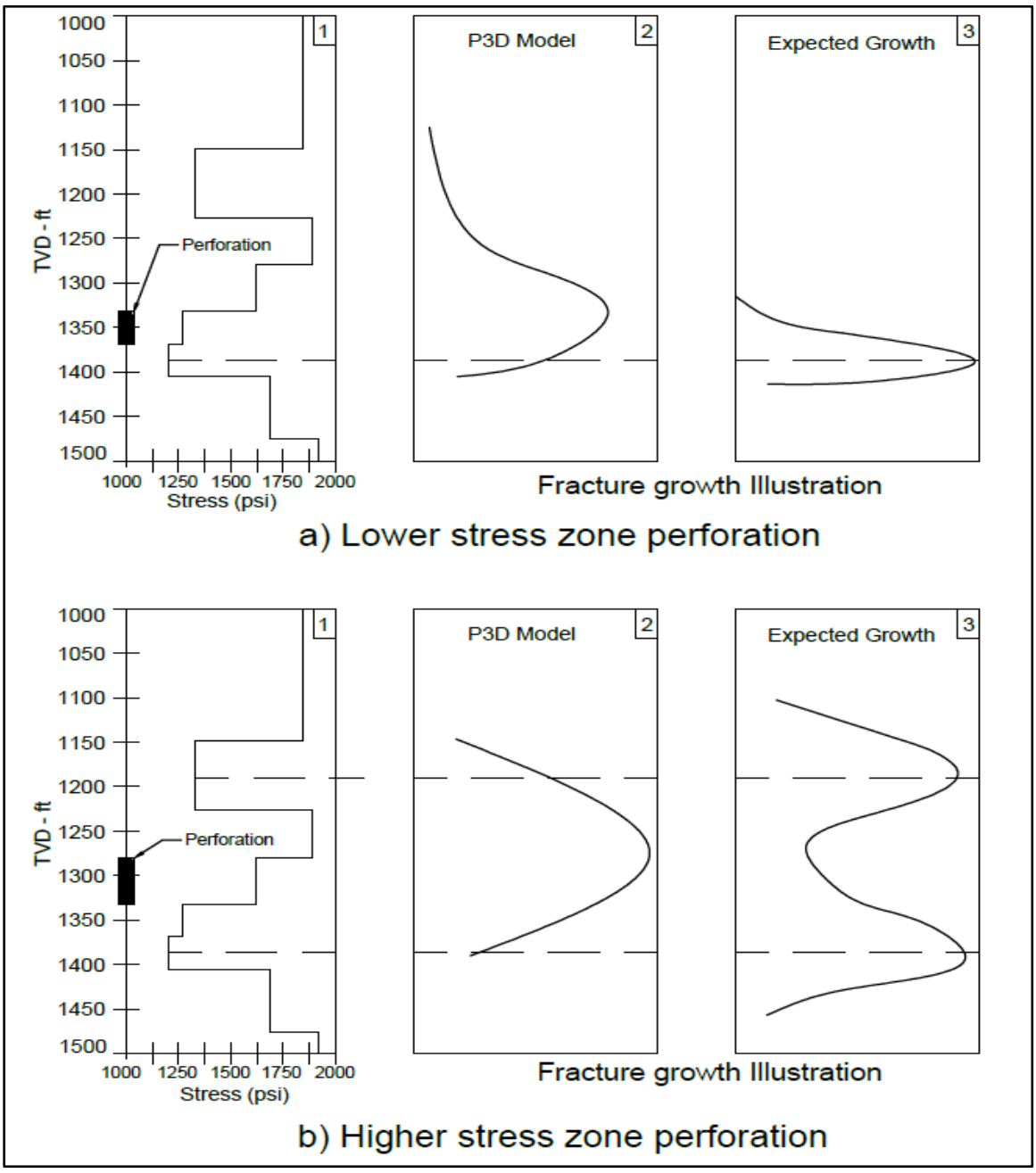

Figure 2.2. Perforation examples in a lower (a) and higher (b) stress zone. Perforations are located outside the lowest stress zone in both instances. The P3D model commonly leads to two common growth occurrences: 1) runaway height growth and 2) uncorrected height growth. The fracture is more likely to be contained or split into more than one propagation front in realistic occurrences (proven from planar 3D simulations).

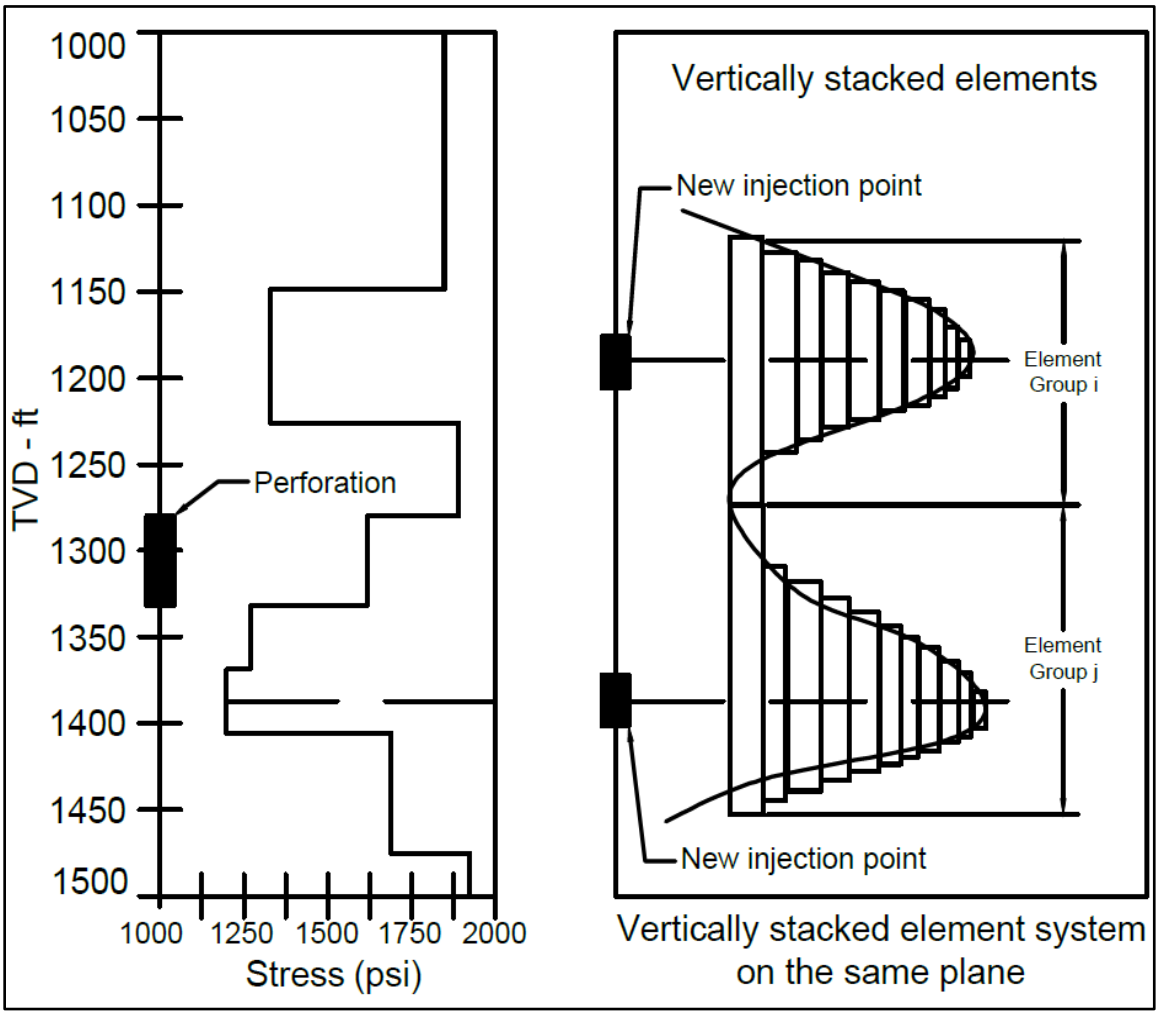

Figure 2.3. Stacked height growth model example illustration. The original injected perforation and eliminated and two new injection points are generated in locations containing the lowest stress zone. It is possible for splitting to occur again if the new injection zones have height growth into other lower stress zone.

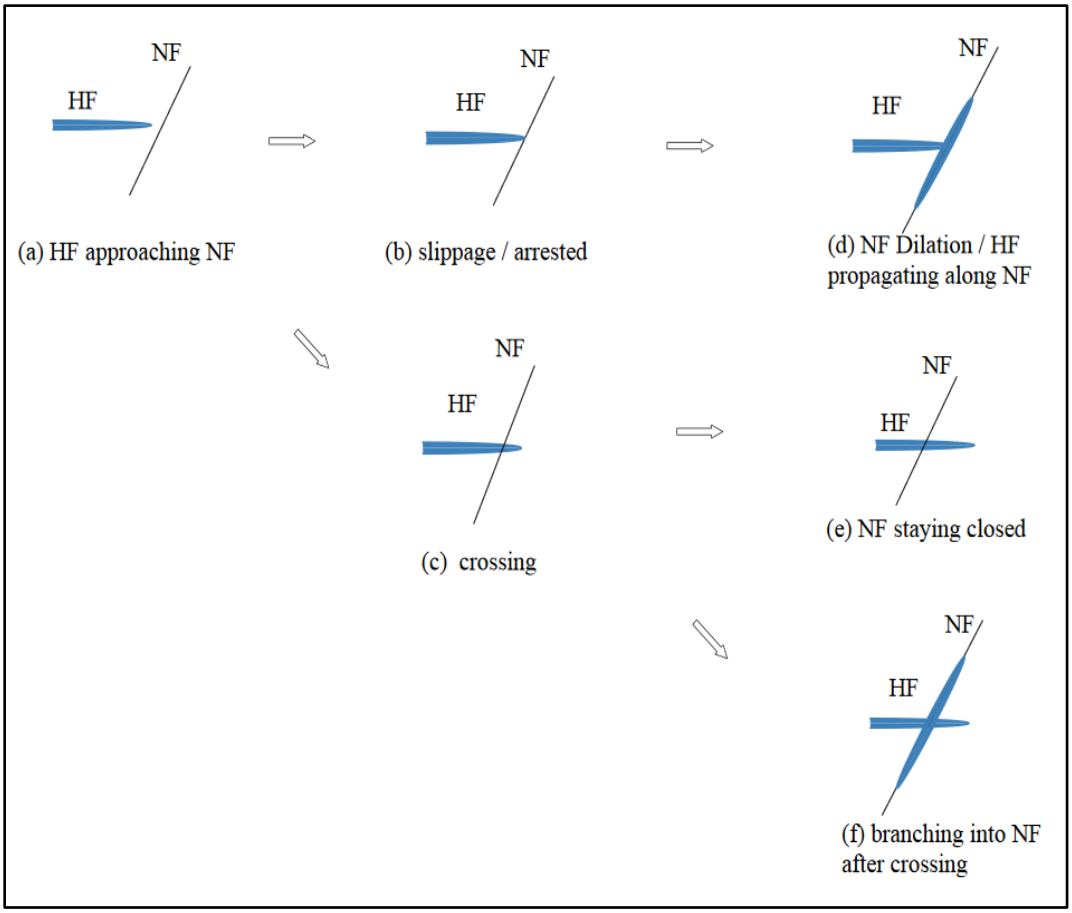

Figure 2.4. Possible hydraulic fracture and natural fracture interactive pathing (modified from Gu, H. et al. (2011) [23]).

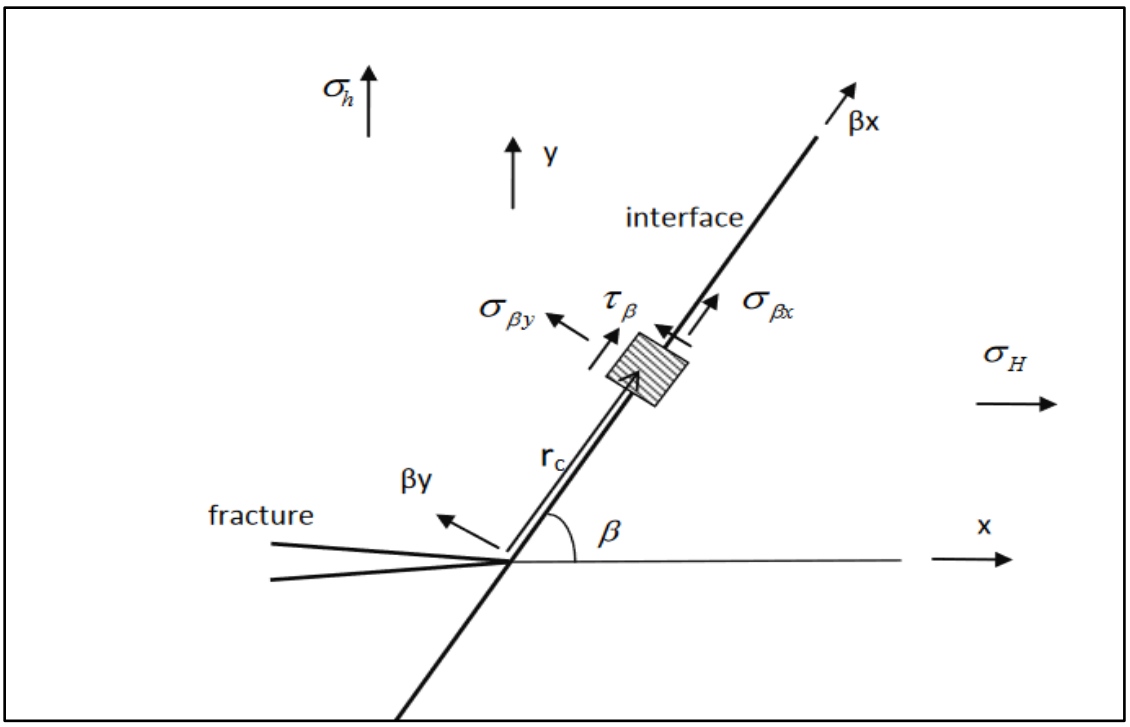

Figure 2.5. Hydraulic and natural fracture stresses and angles of interaction (modified from Gu, H. et al. (2011) [23]).

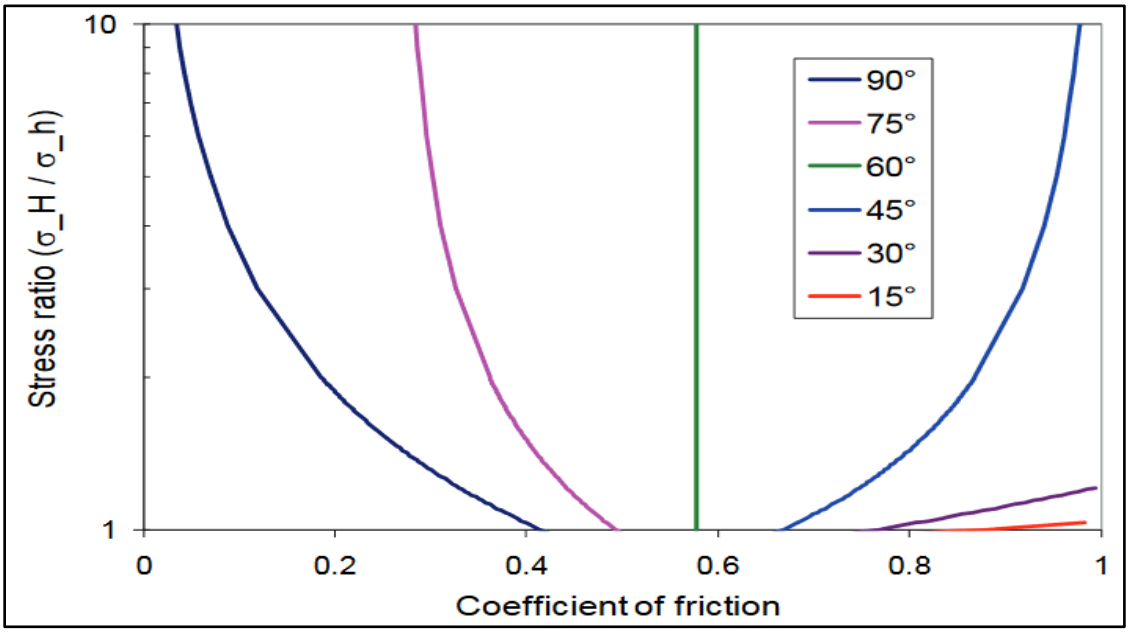

Figure 2.6. Natural and hydraulic fracture crossing criteria. The crossing case is for T0=S0=0 and stress ratio > 1 at different angles of intersection. Any value to the right of a curve defines regions where crossing will occur. As the angle of intersection β decreases, the coefficient of friction μ must be higher for crossing to be possible.

CHAPTER 3

STOCHASTIC MODEL ASSEMBLY

Understanding the subsurface geology is vital in constructing an accurate discrete fracture network (DFN) model. The model will act as the core testing component when analyzing parameter variations in pump schedules and completions designs. It is important that field data provide adequate information to build a model similar to actual geologic structures and their associated mechanical properties.

The first six to eight months of the project focused on data collection and analysis. Subsurface data consisted of:

- Well logs
- Lateral FMI logs
- Diagnostic fracture injection tests
- Drilling completion reports
- Geosteering reports
- Core tests

The information originated from three near-field wells and the three test wells. The near-field wells produce from the same reservoir as the test wells. However, depositional shifts in the lithology is present and will require calibration to the test wells.

Chapter 3 focuses on the approach to building a stochastic model by processing

available field data. Other important components relating to the drilling and completions planning process are not addressed in this document. However, they are still important operational challenges to consider outside the scope of this project. Additional publications can be found in published literature [29-31].

3.1 Well construction

The initial workflow process in FracMan and Mangrove require the construction of a subsurface well. Geosteering and survey reports were available for one wellhead containing three lateral sections. For proprietary purposes, the wells designations are test well 1, 2, and 3 and contain the following design:

- Test Well 1 – Limited entry design
- Test Well 2 – Standard completions design
- Test Well 3 – Standard completions design

Figure 3.1 and 3.2 provided Schematics of the wells. Table 3.1 lists approximate depths, kick-off points, and lengths of the laterals. A well model has been built from referenced geosteering coordinates and tested cross platform between the two fracture simulator packages (Figure. 3.3). Wellhead locations and depths are exact and remain fixed for the entirety of the simulation process.

3.2 Well logging overview

Well placement is highly dependent on petrophysics. It may not be something a drilling and completions engineer is directly involved in. However, it is key to understand how well logging data leads to preplanning designs and corrections during drilling.

Wireline instruments were run down the hole on an electric cable to perform well logging after drilling the well. Open-hole (casing and cement not yet placed) logging was conducted on the test well. The remaining sections provide a general summary of the types of well logs issued and how they affected design choices for the stochastic model.

- Gamma ray

Rocks contain natural occurring radioactive material mostly consisting of potassium, uranium, and thorium. Gamma ray tools measure the amount of natural gamma rays emitted by the rock surrounding the tool. The unit of measurement is API or GAPI, a unit based off the radiation of a concrete block that is nearly twice the radioactivity of any shale rock. It is probably the most commonly used tool for determining changes in lithologic zones. Generally, the gamma ray value is said to be proportional to the amount of shale in the rock. As a rule of thumb, a higher gamma ray means more shale. A spectral gamma ray was also available. The composite results showed nearly the same output as the basic gamma ray, meaning no radioactive discrepancies were present in the logged formations.

- Density log

Density logging also utilizes gamma rays by sending a gamma ray into a formation and recording the amount scattered back. The average electron density in a formation dictates the amount of gamma rays scattered back to the tool. The electron density strongly correlates to the bulk density of the material. A correlation can be made between the scattered gamma ray and bulk density of the nearby rock formation. The unit of measurement for bulk density is in g/cc. Density logging was also used to calculate the density rock porosity.

- Resistivity log

Resistivity logging measures the electrical resistivity of a rock by recording how much a material opposes the flow of electrical current. Resistivity uses multiple pads to eliminate the resistance of the contact leads. The unit of measurement is in Ohms. Hydrocarbons increase resistivity more compared to water. The following provides a general rule:

  - High resistivity high porosity –Likely hydrocarbon
  - Low resistivity high porosity – Likely shale or water

- Neutron log

The neutron-porosity logging is a simple tool. It uses an isotopic source and two neutron detectors similar to density logging. The tool measures the size of the neutron cloud by characterizing the falloff of neutrons between the two detectors. The log targets the average hydrogen density of the material logged. The hydrogen index will track the porosity if all the hydrogen in the formation is in the form of porosity-filling liquid (in particular water or oil).

The density and neutron porosity logs are overlaid on the same track. The key areas of interpretation are regions where the neutron and density porosity logs cross over. Hydrocarbons exist in the zone where the resistivity is high and the porosity logs cross over.

- Sonic log

Sonic logs measure the interval transit time of a formation. The transit time describes a formation's capacity to transmit seismic waves. Seismic wave travel speeds will vary with lithology and rock textures. Travel time is typically faster as rock density

increases. A shear and compressional travel time value was measure and provided. With these data and density logs, geomechanical properties such as Young's modulus, Poisson's ratio, and the in-situ stresses can be solved.

Logging gives valuable information on every formation logged. This information aids in preplanning and optimization during drilling. Logging provides the information necessary for the following:

- Identify subsurface formations and their thicknesses
- Estimate regions with gas and oil in place
- Determine geomechanical rock properties
- Choose proper casing placement

3.3 Stratigraphy

Subsurface model layers were built based on user selected interval changes from the gamma ray. Vertical openhole logs were not run in the test wells. Consequently, available vertical well data were given from three nearby wells designated as near-field 1, 2, and 3. Figure 3.4 provides a map of the location of the wellheads. Gamma ray correlations of the near-field wells are illustrated in Figure 3.5. The yellow line represents the known payzone depth that is used as the matching region between logs. The boxed regions are where core samples were extracted. The objective consisted of matching the gamma rays of the near-field wells to the test well mud log, verifying that the gamma ray patterns are similar between wells, and picking stratigraphic changes as a function of depth.

Mangrove and FracMan require the user to input the TVD and the thickness of each formation. The operator engineers and geologists suggested a simple lithological model

100 ft. above and below the payzone. The decision was based on fracture height growths from previous stimulation jobs not escalating above 50 ft and below 20 ft. The hindrance in height growth is possibly be due to lamination effects. It requires a high amount of energy to vertically fracture through additional beddings. Multiple interbedded formations were observed from the gamma ray logs. Thirty layers were identified ranging from 5-20 ft in bedding thickness within the 200 ft interval. Figure 3.6 illustrates a side view of the vertical stratigraphy matched to the test wells. The next step requires populating the layers with geomechanical properties.

3.4 Rock properties

Goemechanics is a fundamental building block in drilling and completions, yet not fully utilized in drilling and completions. This may be due to limited availability in well logs necessary to perform petrophysical analysis. Understanding the mechanical behavior of a rock allows an engineer to make reasonable influential choices during phases of completion, stimulation, and production.

Rock characteristics were loaded into the layers surrounding the lateral. As a result, the containing layer rock property data are used in the equations defined in Chapter 2 during each time step of the simulation. The properties input into stratigraphic zones were:

- Minimum horizontal stress(σ_3)
- Maximum horizontal stress(σ_2)
- Overburden stress (σ_1)
- (σ_1) Trend/plunge
- (σ_3) trend/plunge

- Young's Modulus
- Poisson's ratio

The methods to calculating each value are listed in the following sections. Petrophysical analysis techniques are referenced from Crain's Petrophysical Handbook [32].

- Poisson's ratio

$$\nu = \frac{\left[0.5\left(\frac{DTS}{DTC}\right)^2 - 1\right]}{\left[\left(\frac{DTS}{DTC}\right)^2 - 1\right]} \tag{3.1}$$

- ν.....Poisson's ratio
- DTS .....Compressional travel time (μsec/ft),
- DTC .....Shear travel time (μsec/ft)

- Shear modulus

$$G = 13{,}400\left(\frac{RHOB}{DTS^2}\right) \tag{3.2}$$

- G ..... Shear modulus (x106 psi),
- RHOB .....Formation density log (g/cc)

- Young's modulus

$$E = 2G(1+\nu) \tag{3.3}$$

  - E.....Young's modulus (x106 psi)

- Bulk modulus with porosity

$$K_b = 13{,}400 * RHOB\left(\frac{1}{DTC^2} - \frac{3}{4}\frac{1}{DTS^2}\right) \tag{3.4}$$

  - Kb .....Bulk density with porosity (x106 psi)

- Bulk modulus with no porosity

$$DENSMA = \left(\frac{RHOB - PHIT * DENSW}{(1-PHIT)}\right) \tag{3.5a}$$

$$DTCMA = \left(\frac{DTC - PHIT * DTW}{(1-PHIT)}\right) \tag{3.5b}$$

$$DTSMA = \left(\frac{DTS}{(1-PHIT)}\right) \tag{3.5c}$$

$$K_m = 13{,}400 * DENSMA\left(\frac{1}{DTCMA^2} - \frac{3}{4}\frac{1}{DTSMA^2}\right) \tag{3.5d}$$

- Km .....Bulk density without porosity (x106 psi),
- PHIT .....Total porosity (fraction),
- DENSW ..... Density of the fluid in the rock pores (g/cc),
- DTW .....Travel time through the fluid in the rock pores (μsec/ft)

- Biot's constant

$$B = 1 - \left(\frac{K_b}{K_m} \right) \tag{3.6}$$

- B.....Biot's constant (unitless)

- Overburden pressure gradient

$$\sigma_v = \frac{0.0605 * SUM(RHOB_i * INCR)}{DEPTH} \tag{3.7}$$

- σv ..... Overburden pressure gradient (psi/ft),
- RHOBi .....Formation density log reading at *i*-th data point(g/cc)
- INCR..... Digital log data incriment (psi/ft),
- ,DEPTH ..... Logging depth (ft)

- Pore pressure gradient

$$\sigma_{pore} = \frac{DENSW}{DEPTH} \tag{3.8}$$

- σpore .....Pore pressure gradient (psi/ft),
- RHOBi .....Formation density log reading at *i*-th data point(g/cc)

- Minimum stress gradient

$$\sigma_{\min} = \left(\frac{\nu}{1-\nu}\right)\left(\sigma_v - B*\sigma_{pore}\right) + B*\sigma_{pore} \tag{3.9}$$

- σmin ..... Minimum horizontal stress gradient (psi/ft)

- Maximum stress gradient

$$\sigma_{\max} = \sigma_{\min} * Correction \tag{3.10}$$

- σmax .....Maximum horizontal stress gradient (psi/ft)

Rock properties were calculated from near-field well 3 and correlated to the test wells. Figures 3.8, 3.9, and 3.10 provide values for the Poisson's ratio, Young's modulus, and minimum horizontal stress. Regions with no data or outliers are locations where logging stopped. Instances with no data required referencing from the core samples and DFIT reports. The most important region, the payzone, was one of these cases. However, rock core samples were extracted at the payzone depths and tested (red region Figure 3.10). The geomechanical properties were within reason compared to the logging calculations. Final rock values were integrated into the layer properties used for later simulations.

3.5 Complex natural fracture sets

Halliburton provided the fracture count and orientation data processed from the FMI logs from test well 2. Approximately 1800 conductive fractures (fractures of interest) exist in the lateral. No noticeable faults were identified in this area of the field. The fracture orientations fall into two major groups: NW and SE groupings (conjugate fracture systems). The fracture set data were uploaded into FracMan and verified using a stereonet plot and Rose plot comparison between the raw Halliburton data and statistically generated fractures (Figure. 3.7). Then, the fracture set mean pole/trend was approximated. The accuracy of the mean pole/trend calculated from the data was validated by running an internal FracMan routine. The algorithm is a probabilistic pattern recognition algorithm that defines fracture sets from field data.

The actual fracture data are not used for simulations in FracMan. The software requires a theoretical fracture set to be statistically generated from user-defined input. The fracture sets required inputs for the fracture intensity (P10) and mean pole/trend. Two fracture sets were produced using the data input from the Halliburton FMI evaluations.

The fracture sets are generated in a bounded region. In this instance, the selected region surrounded the lateral section of the well. The statistical routine in FracMan generated approximately 100,000 – 250,000 fractures. The region was filtered to only include fractures that directly connected to the well. The filtered connected fracture set count and location was nearly identical to the conductive fractures input from the FMI data, as would be expected. Essentially, a realistic set of natural fractures was generated along the length of the wellbore. Figure 3.8 shows a 2-dimensional visualization of the fractures that were generated along the length of the wellbore and imported Mangrove.

3.6 Completions and treatment design

The baseline treatment design was copied from postfracture reports for well 1, 2, and 3. To avoid confusion, each isolated and perforated well section that is treated individually will be called a stage. Steps in the treatment schedule where there is a change in rate, fluid, additives, or solids added is classified as a sequence. The treatment schedule consisted of 33 sequences including HCl, slickwater, and HCl-gelled acids, diverter, and perforation plugging materials. Sequences were placed into three groupings (Table 3.2).

The fracture design used Ranch House medium rock salt as diverting agent. Diverter was pumped in sequences 5, 14, and 22 (Table 3.2). Diversion is not specifically represented in this or other multiple fracture simulators and required some creative (but rational) simulations. Diversion was numerically modeled by pumping proppant with similar size and density of the rock salt. The simulation is temporarily terminated and properties are recorded in fractures taking fluid and proppant once fluid is finished pumping through a grouping. Fractures that took proppant were eliminated (i.e., no further injection will occur into those because they have been assumed to have been blocked by diverter). The modified fracture set is loaded back into the simulation and reinitialized at the beginning of the next assigned grouping in the pump schedule. After completion, the final report results are compiled along with the properties of the fractures removed.

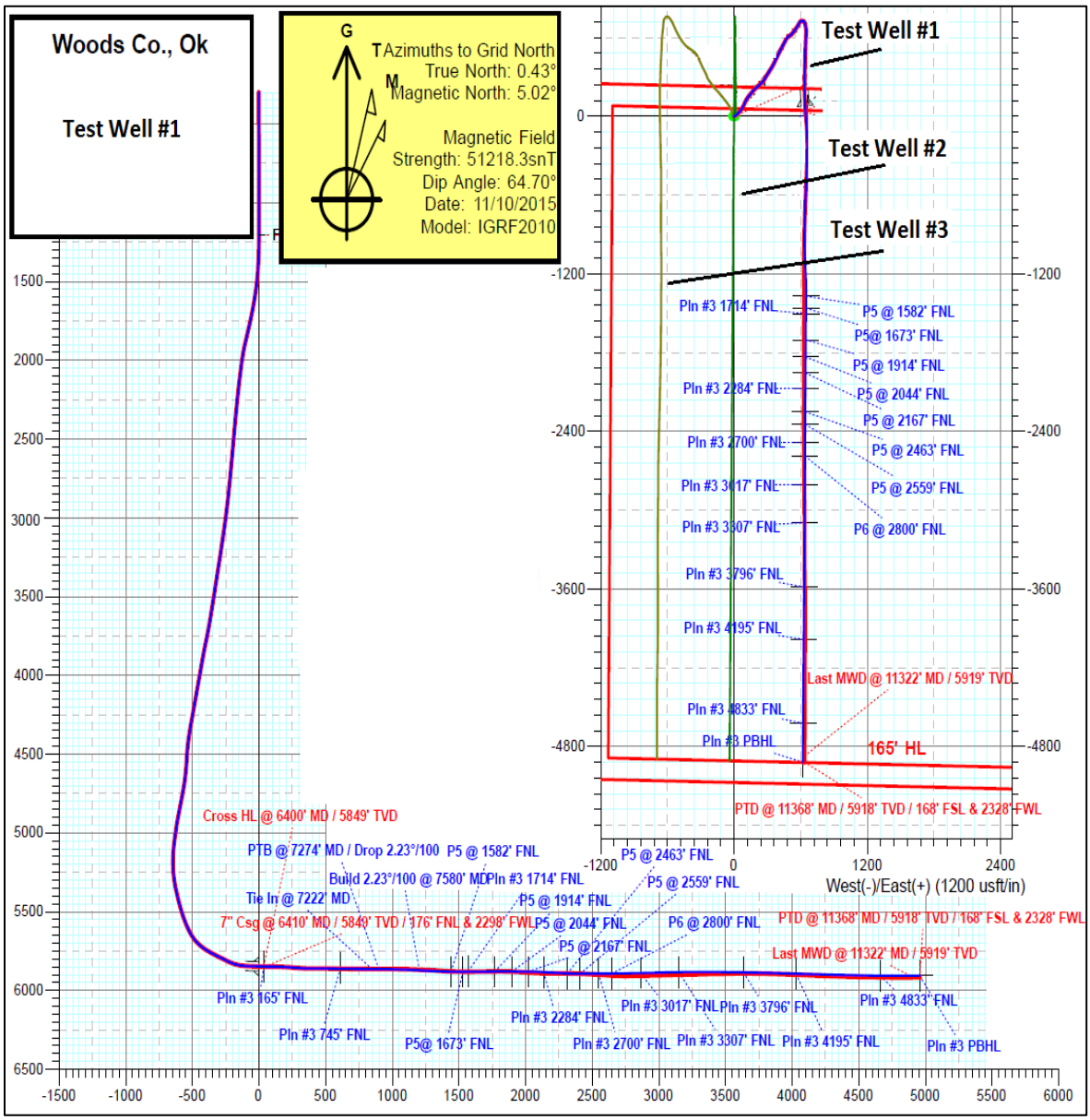

Figure 3.1. Topographic and side well schematics view for the test wells. Test well #1 and #3 will be the new limited entry design and test well #2 remains the standard design.

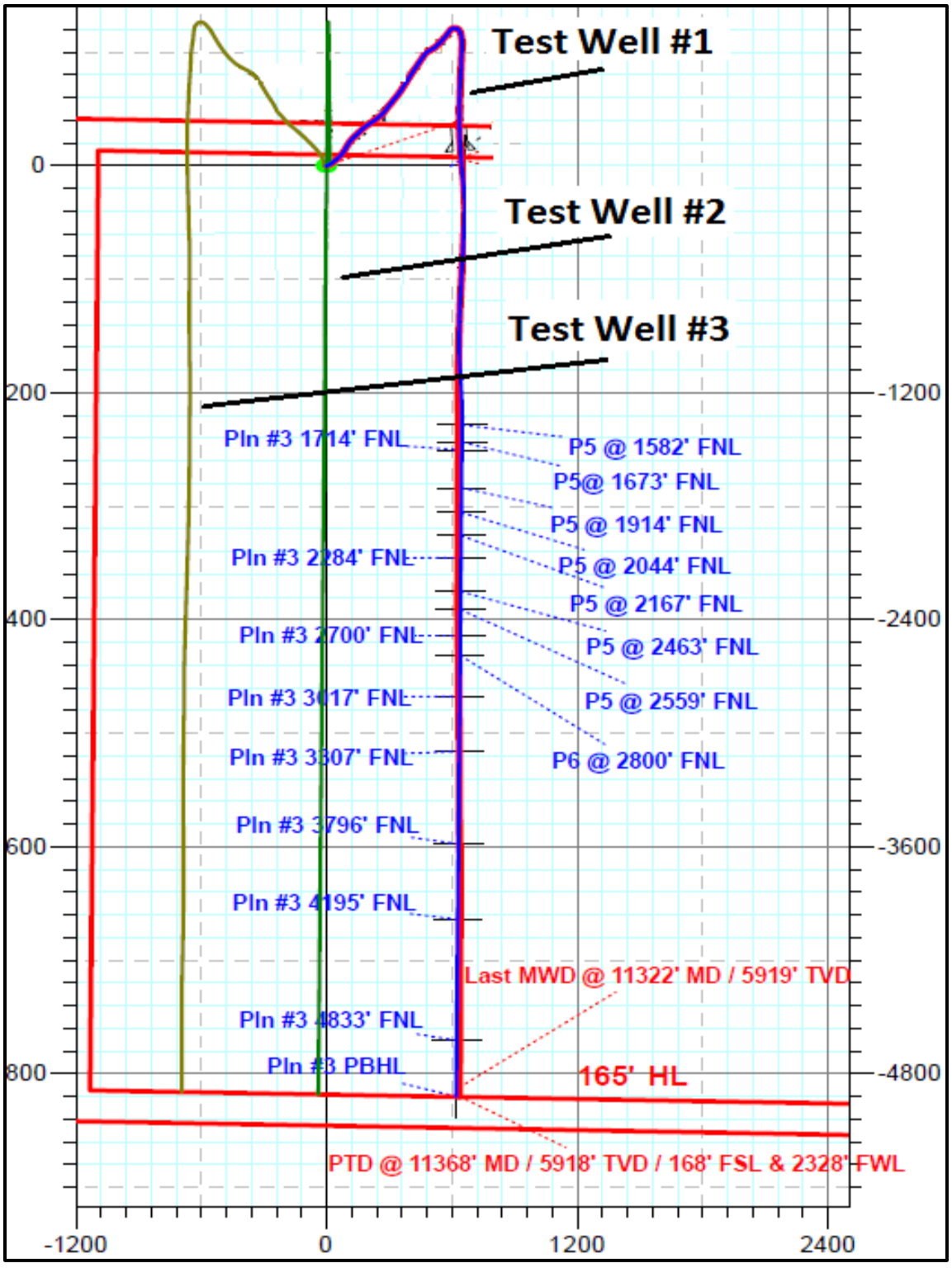

Figure 3.2. Magnified topographic well schematic view for the test wells.

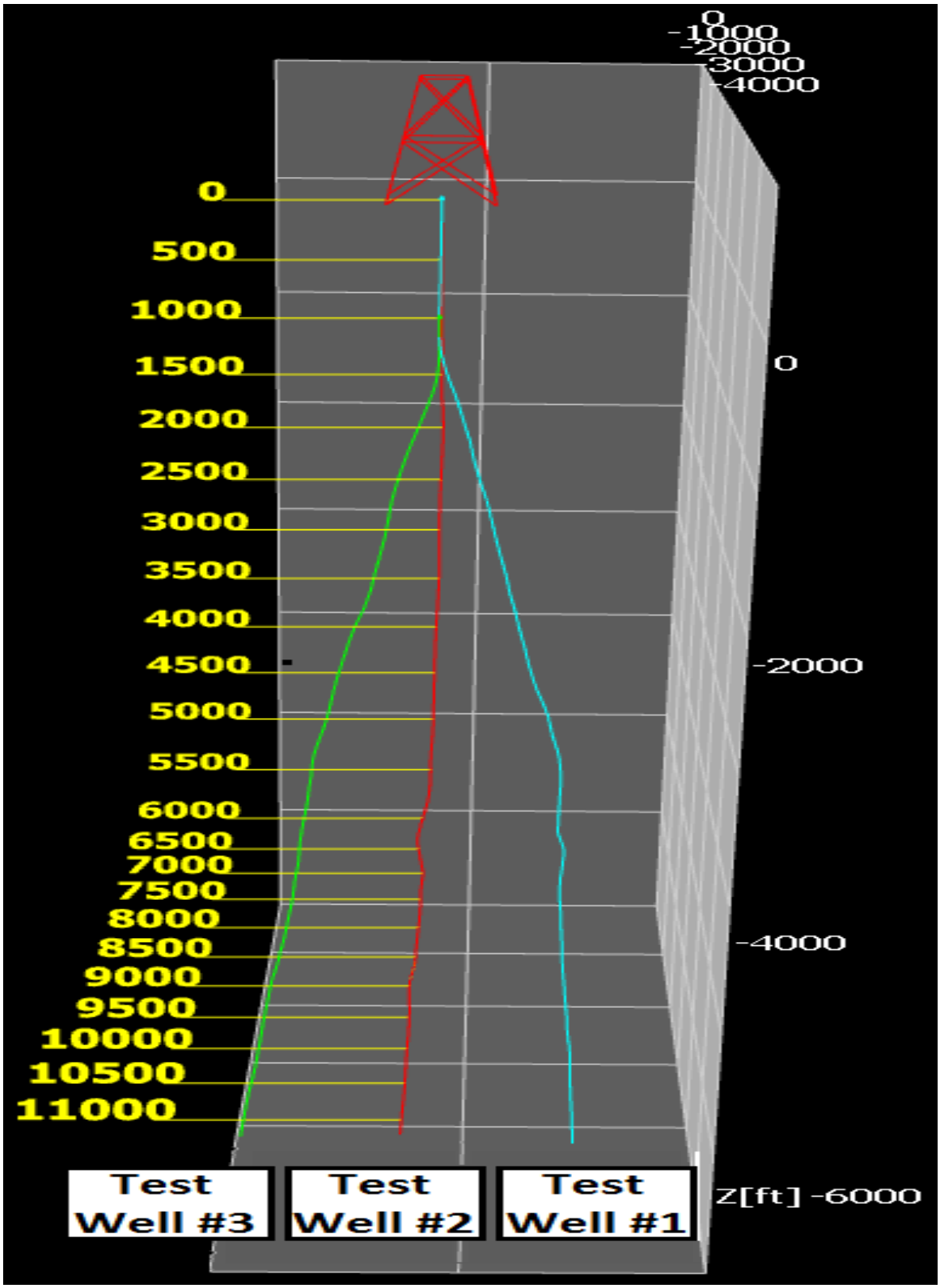

Figure 3.3. FracMan well plan. The well traces have cross platform capability with Mangrove.

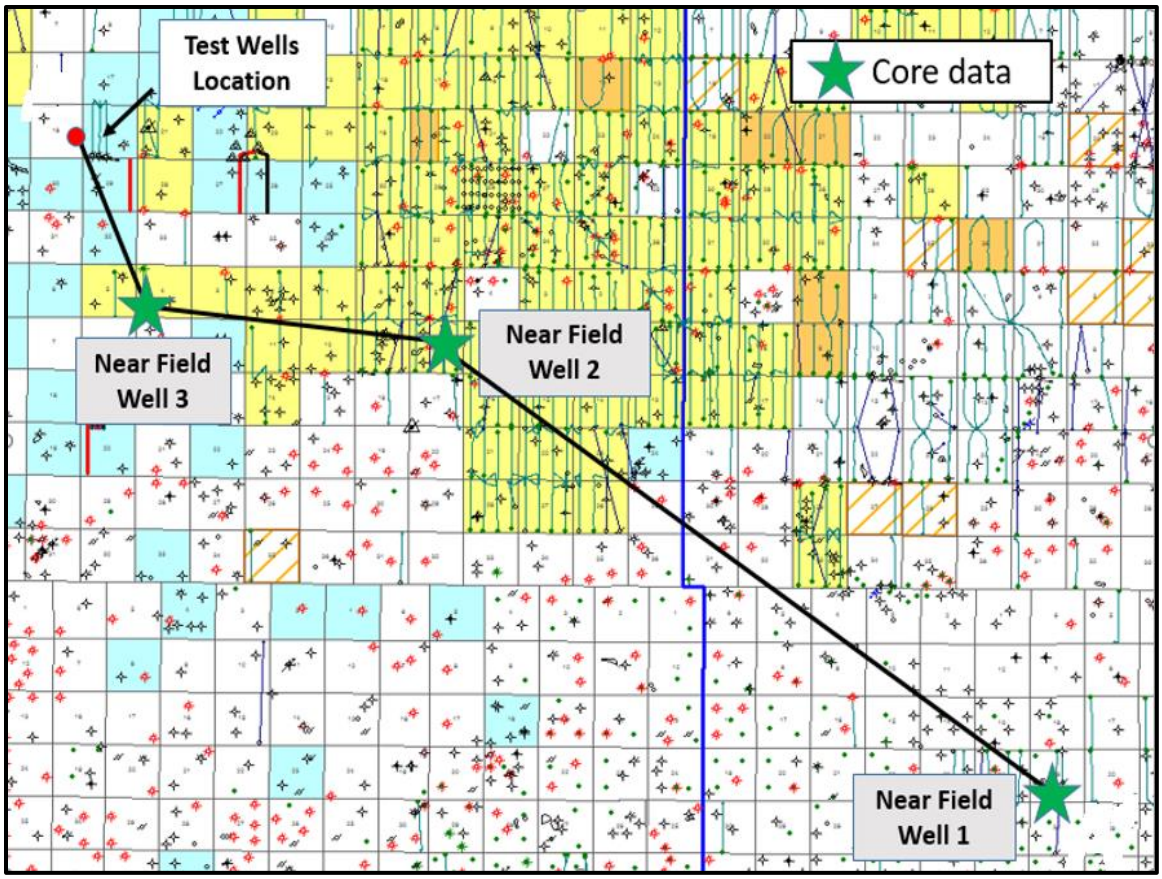

Figure 3.4. Topographic mapping of the test wells and the near field wells. The graphing is used to correlate the subsurface stratigraphy and rock properties. Each square section represents one mi^2.

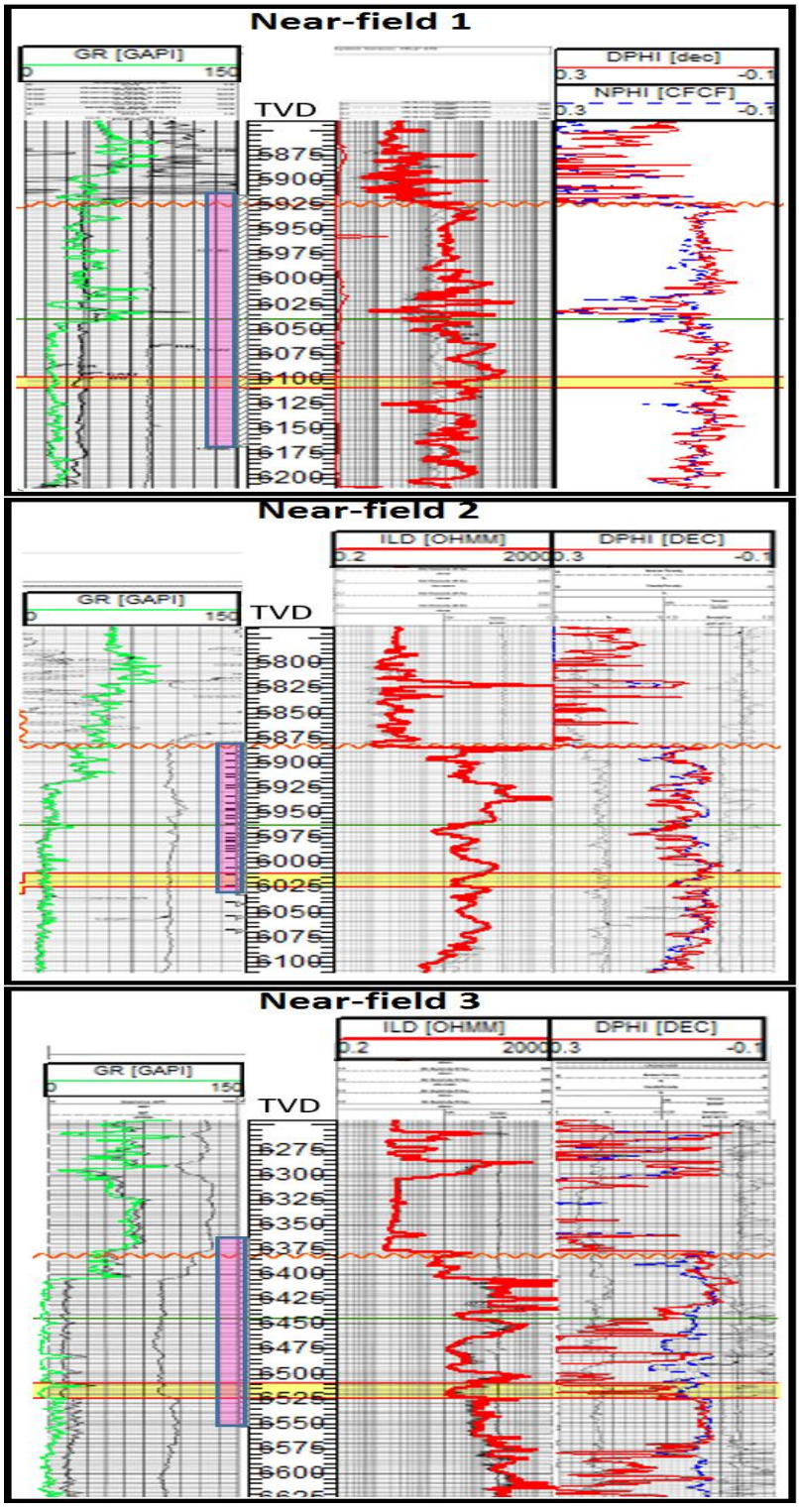

Figure 3.5. Gamma ray and resistivity log matching to the test well payzone. The highlighted yellow region represents the payzone depth. Boxed areas represent depth where core samples were extracted.

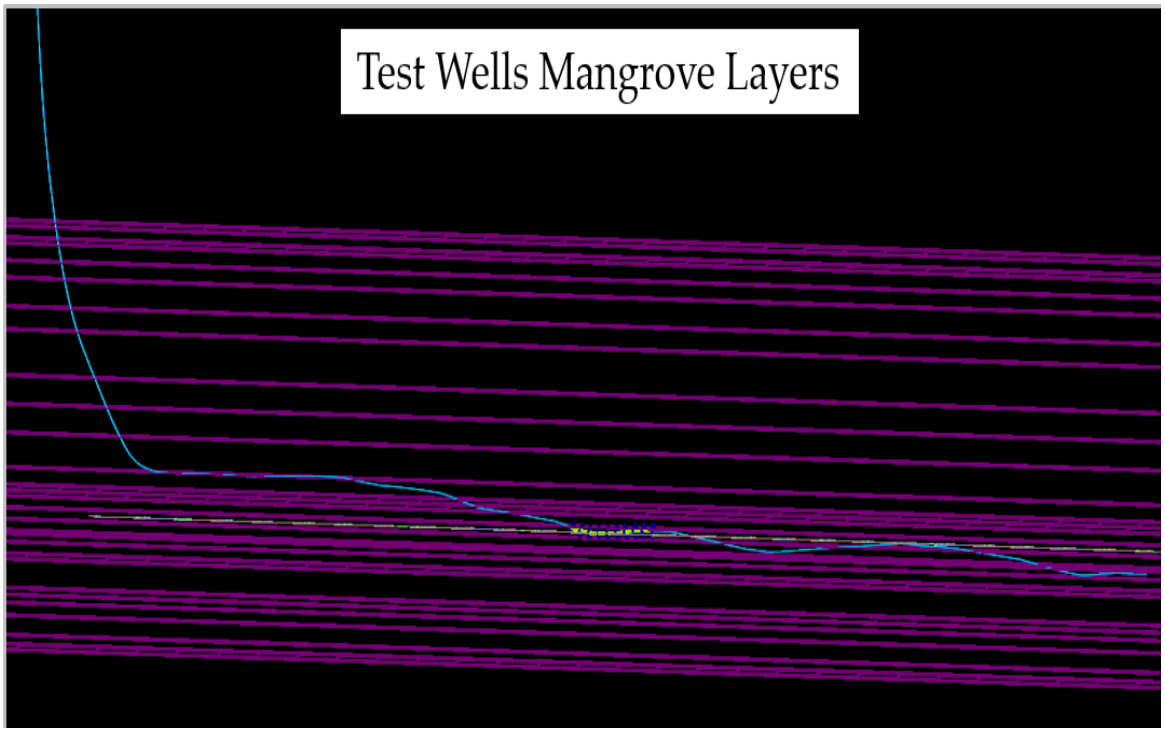

Figure 3.6. Mangrove side view describing test well layer inputs. Thirty layers were selected within a 200 ft. vertical interval. Layer thicknesses ranged from 5-25 ft.

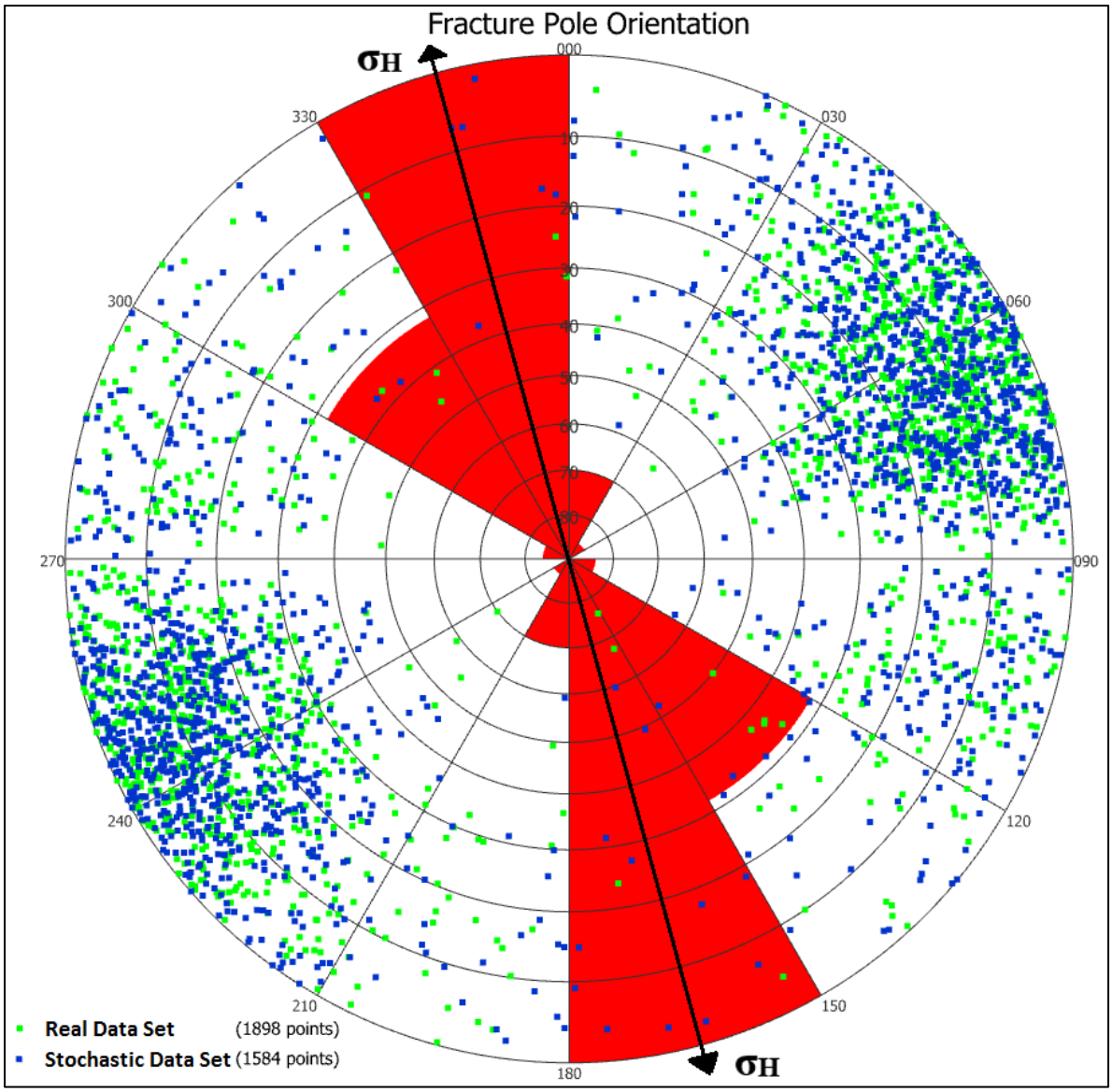

Figure 3.7. Test well #2 stereographic and rose plot. Blue dots represent the generated fracture set and the purple describe the actual FMI fractures. The red region is the rose plot describing the strike and dip of existing natural fractures.

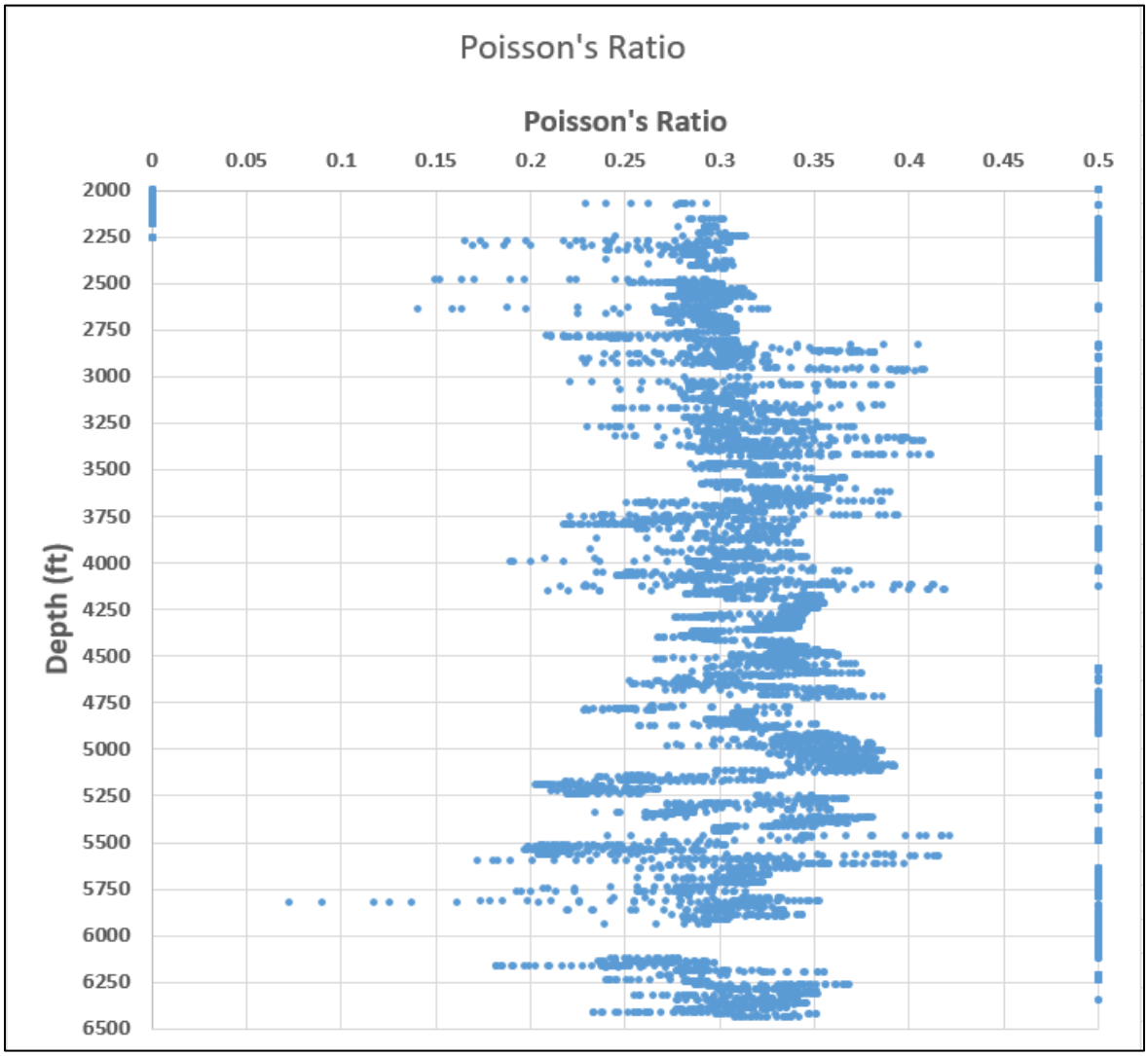

Figure 3.8. Test well Poisson's ratio.

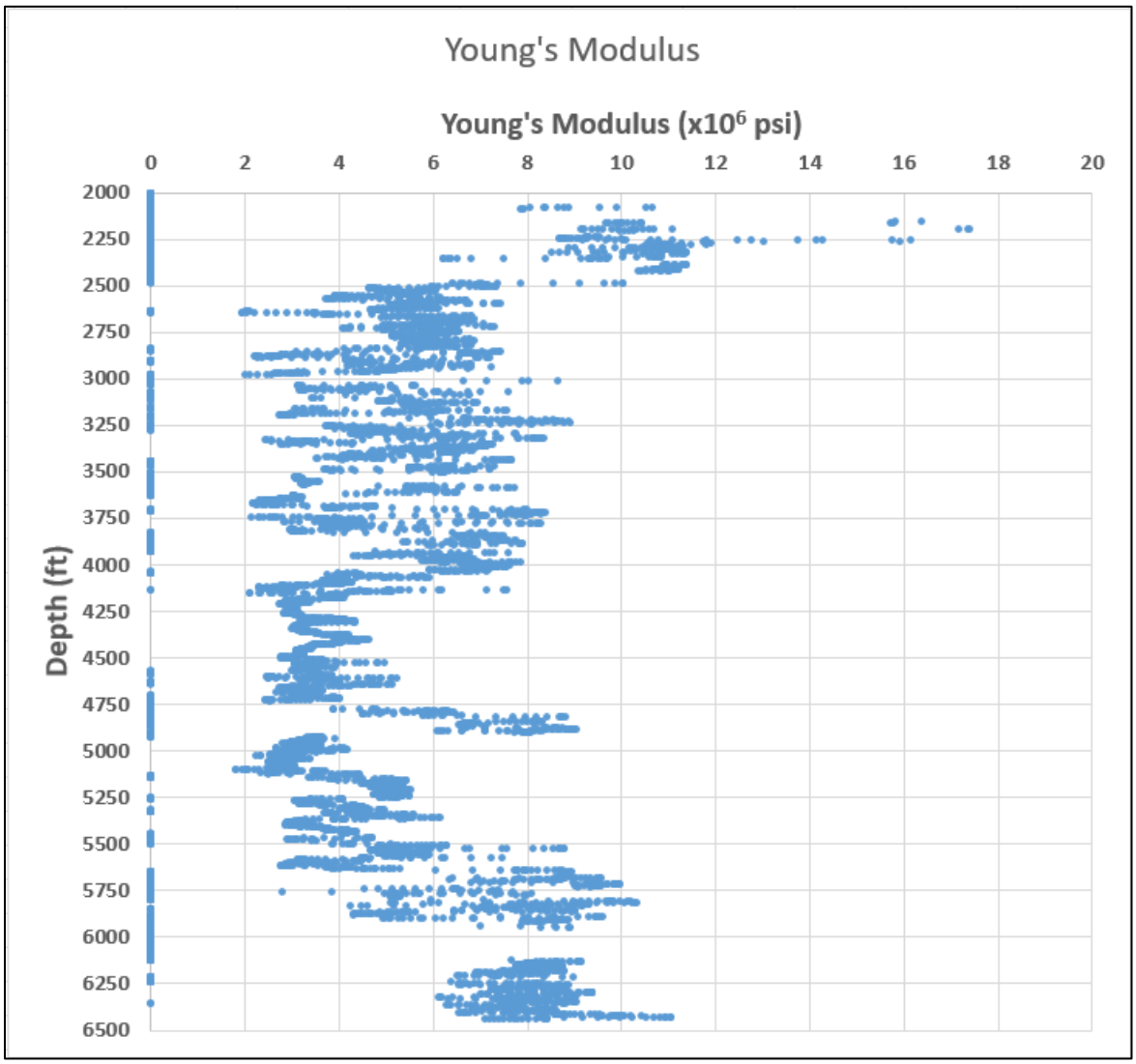

Figure 3.9. Test well Young's modulus.

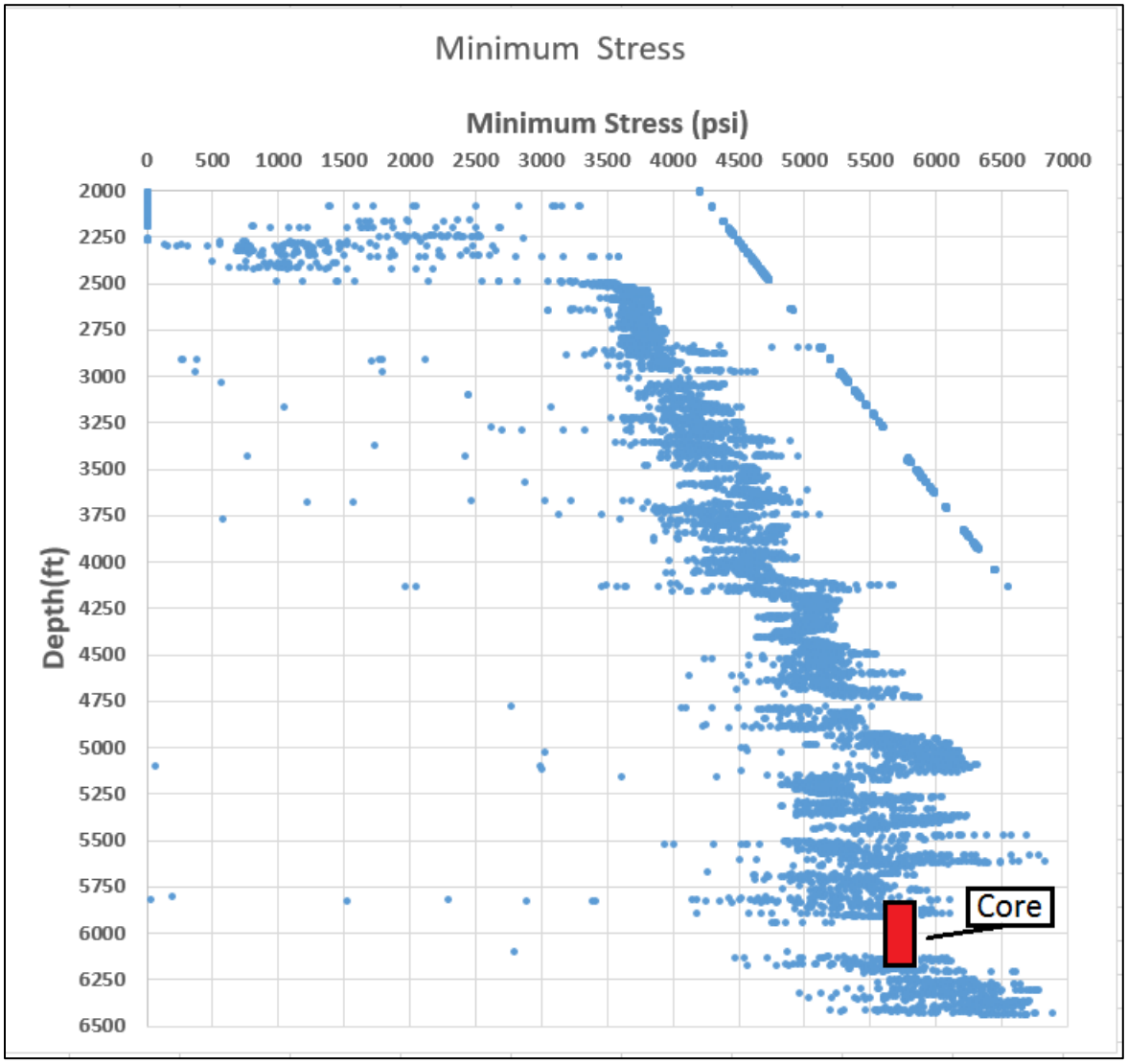

Figure 3.10. Test well minimum horizontal stress. Logging data were not available in the payzone. However, core was taken at the payzone depths. The geomechanical properties were within reason compared to the logging calculations.

Table 3.1: Listing of well depths of interest.

Well Name	Total Length MD (ft)	Kickoff Point MD (ft)	Approximate max TVD (ft)	Lateral Length MD (ft)
Well #1	11322	5092	5919	~5000
Well #2	11198	5092	5915	~5000
Well #3	11411	5092	5916	~5000

Table 3.2: Pump schedule sequence and diverter groupings

Group	Sequences	Sequences with diverter
1	1-7	5
2	8-15	14
3	16-33	22

CHAPTER 4

SIMULATION RESULTS AND ANALYSIS

The final tasks before running the numerical model are calibration and test comparisons. Focus was placed on one fracture stage of test well 2 located approximately at the lateral midpoint. The optimized stage will act as a template for simulating other regions of the lateral and eventually the remaining test wells. Chapter 4 includes model stress tests performed on the well, their results, and three-month production data from the three test wells for model validation.

4.1 Cluster and perforation design

As mentioned, the company of interest wanted to test the feasibility of a limited entry design. This engineered method strategically places the perforations in locations where the well is believed to achieve the most fracture growth, reduce unnecessary treatment pressure, and ultimately minimize inefficient perforations.

Simulations were run on two completion cases: a limited entry design and the standard design. The standard approach has 120 perforations and 4 clusters per fracture stage (300 ft. interval in the stage being assessed). The new limited entry design in the same interval has 10 clusters and 40 perforations. The success of the completions choice was based on the amount of fracture area produced at a given treatment rate. The actual

postfracture report rates during the slickwater and diverter sequences averaged around 100 barrels per minute (BPM) and served as the baseline comparison. Additional variations around the 100BPM rates were run (Table 4.1).

Each simulation was separately ran using the same fracture model. Figure 4.1 posts graphical results of each injection rate. Table 4.2 lists the final job fracture areas from Figure 4.2. The comparison between the 100 BPM limited entry and standard pump schedule is noticeable. There is approximate a 17% increase in fracture growth with the new design. The standard plan is achieving the same output as a ~75 BPM limited entry design.

4.2 Diverter results

Limited entry results showed an improvement to fracture area growth. However, simulations were performed without stopping and reinitiating the process. The workflow plan is to understand rate affects before varying diversion.

The same pump schedule from the completions comparison is used. Rates were fixed at 100 BPM. The diverter (proppant input in the simulator) ranged from 8-14 mesh size. Diverter inputs were varied based on concentration percentage. Table 4.3 outlines the percentages and corresponding concentrations. A 100% concentration correlates to the real-time fracture job.

Fracture area growth based on diversion requires manipulation by the user. Hence, graphical reports are not possible due to constantly terminating and resuming simulations. However, numerical values were saved from the eliminate fractures and were summarized with the final output of the simulation. Table 4.4 lists the results between the limited entry

and standard design at 100BPM based on diverter concentration variations.

A diverter concentration of 0% represents a clean fluid injection. Results indicate that diverter is having an adverse effect on fracture area growth. However, increasing diverter is not inflicting more fracture growth. Results between both completions cases suggest an optimized volume of diverter to fracture area growth relation.

4.3 Well production comparison

Final model validations focus on well production data. Production has been online for three months and been provided by the operator. Figures 4.2-4.5 show the daily and cumulative gas, oil, water, and barrels of equivalent oil (BOE). For reference, the test well completions are as follows:

- Test Well 1 – Limited entry design
- Test Well 2 – Standard completions design
- Test Well 3 – Standard completions design

The overall pay thicknesses of each well is in the following:

- Test Well 1 – 1919ft
- Test Well 2 – 205ft
- Test Well 3 – 1545ft

Test well 1 and 3 had the closest payzone thicknesses and were used for completions comparisons. The limited entry well shows similar three-month cumulative production results compared to the standard design. A noted difference is test well 1 produced approximately 20% less water over the three-month period.

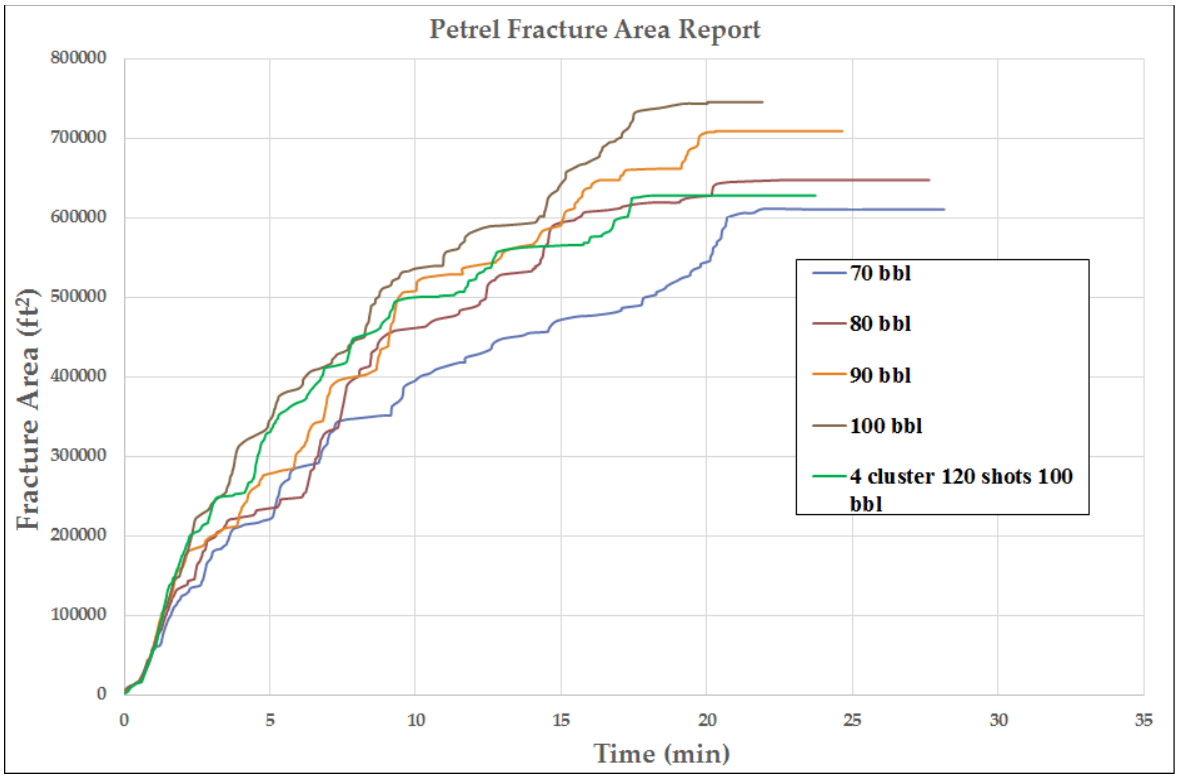

Figure 4.1 Cluster design postfracture area results. The green line represents the standard design treatment results used in the real fracture job.

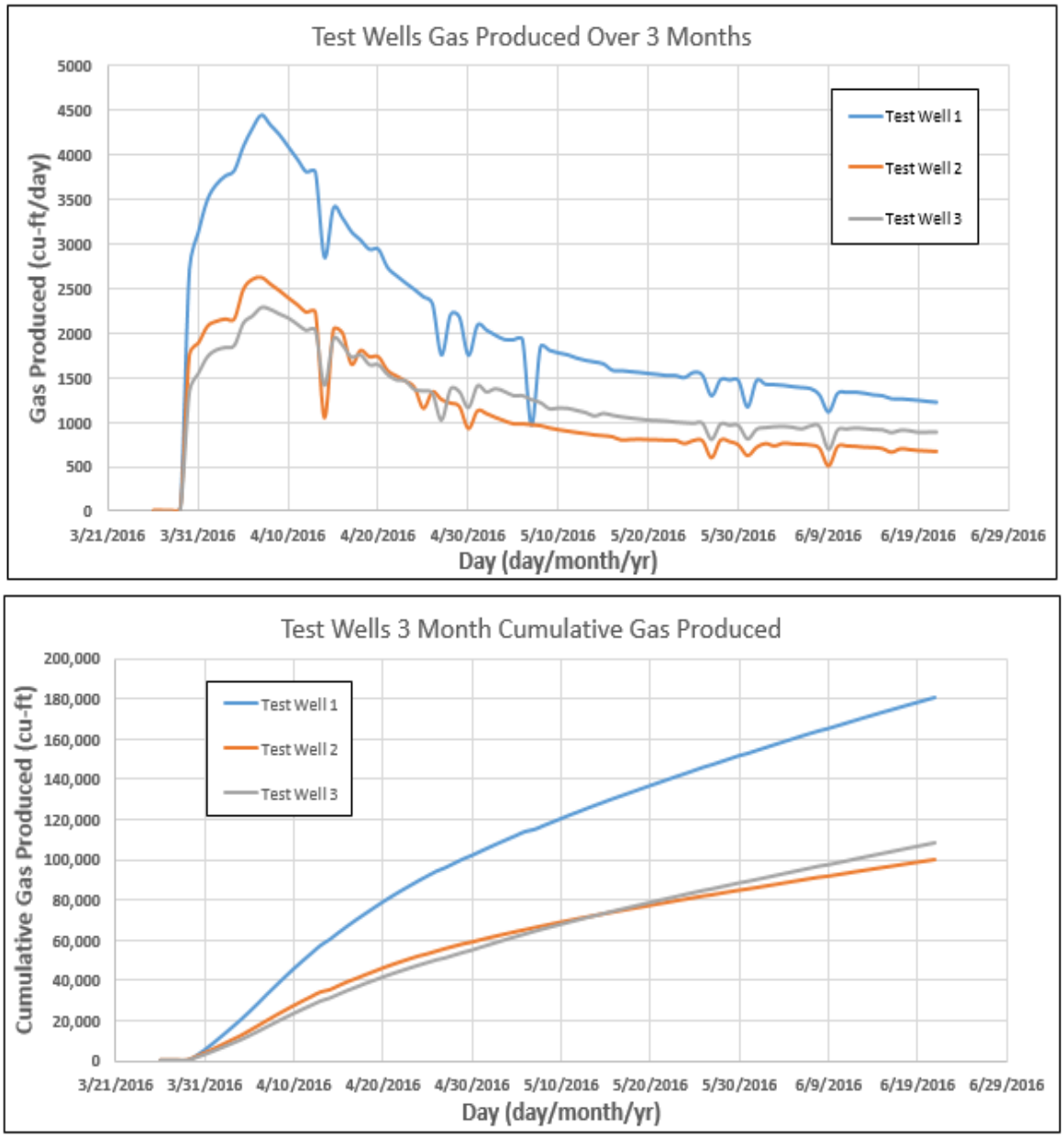

Figure 4.2. Test well three-month daily and cumulative gas production.

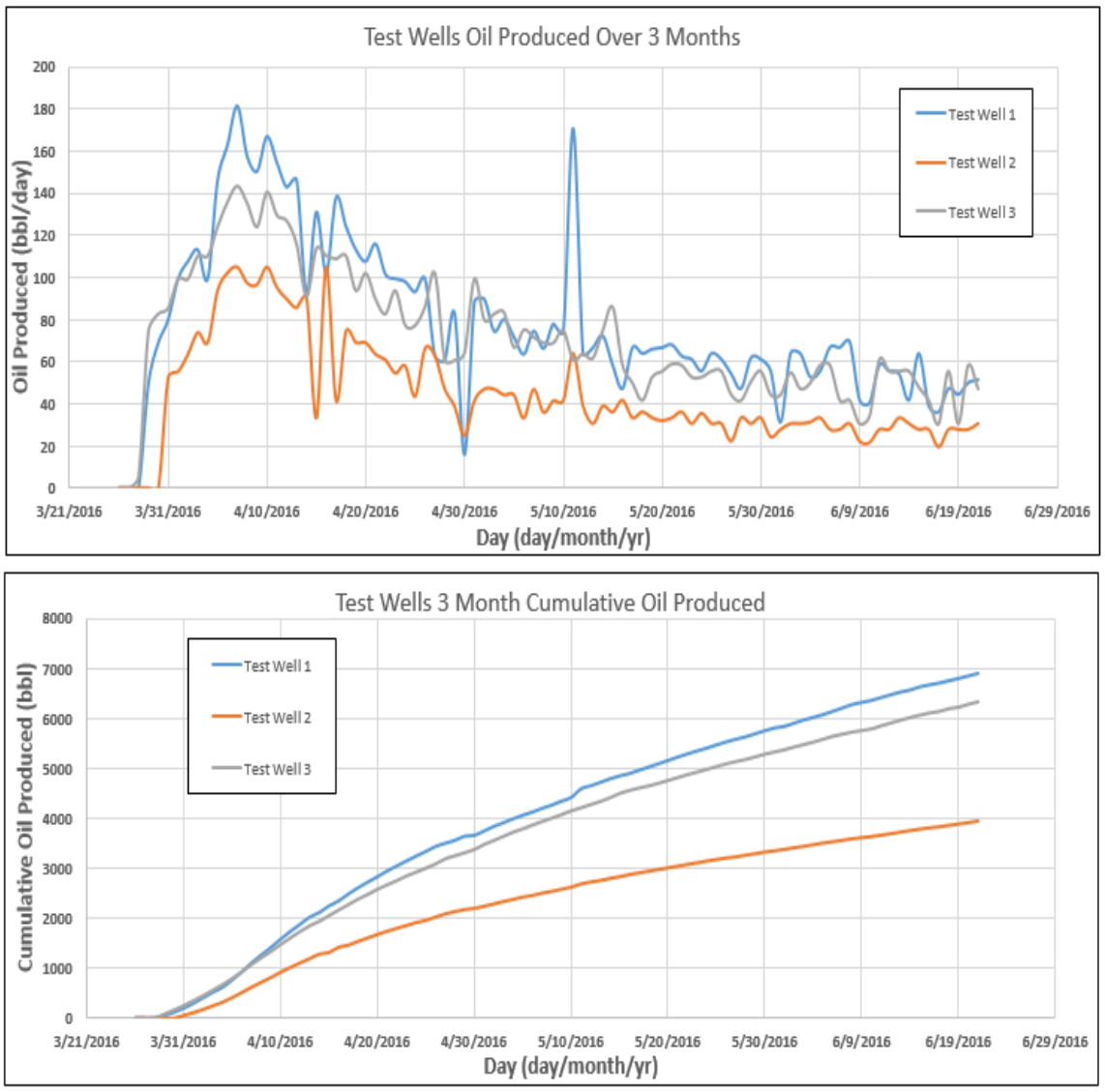

Figure 4.3. Test well three-month daily and cumulative oil production.

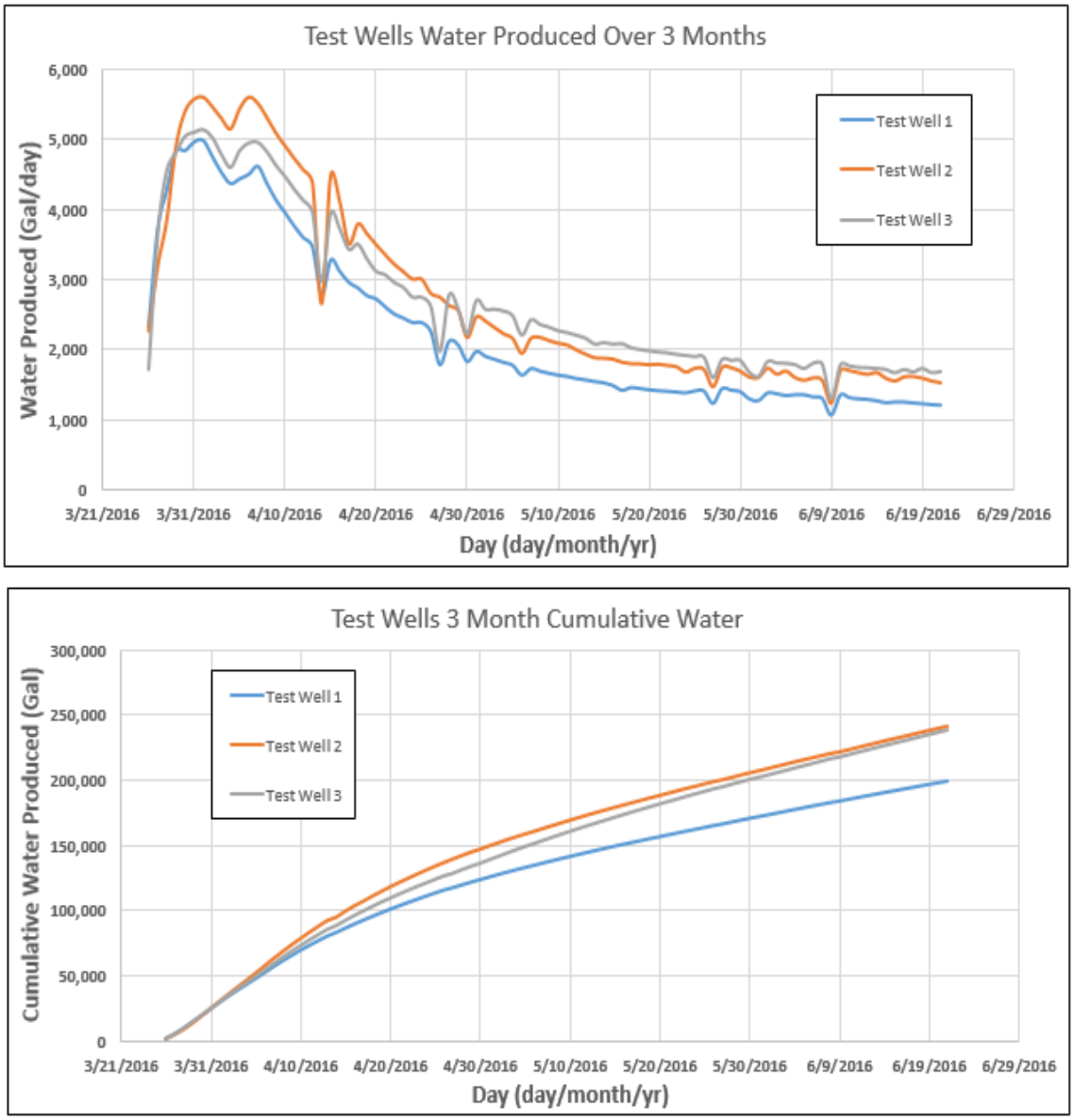

Figure 4.4. Test well three-month daily and cumulative water production.

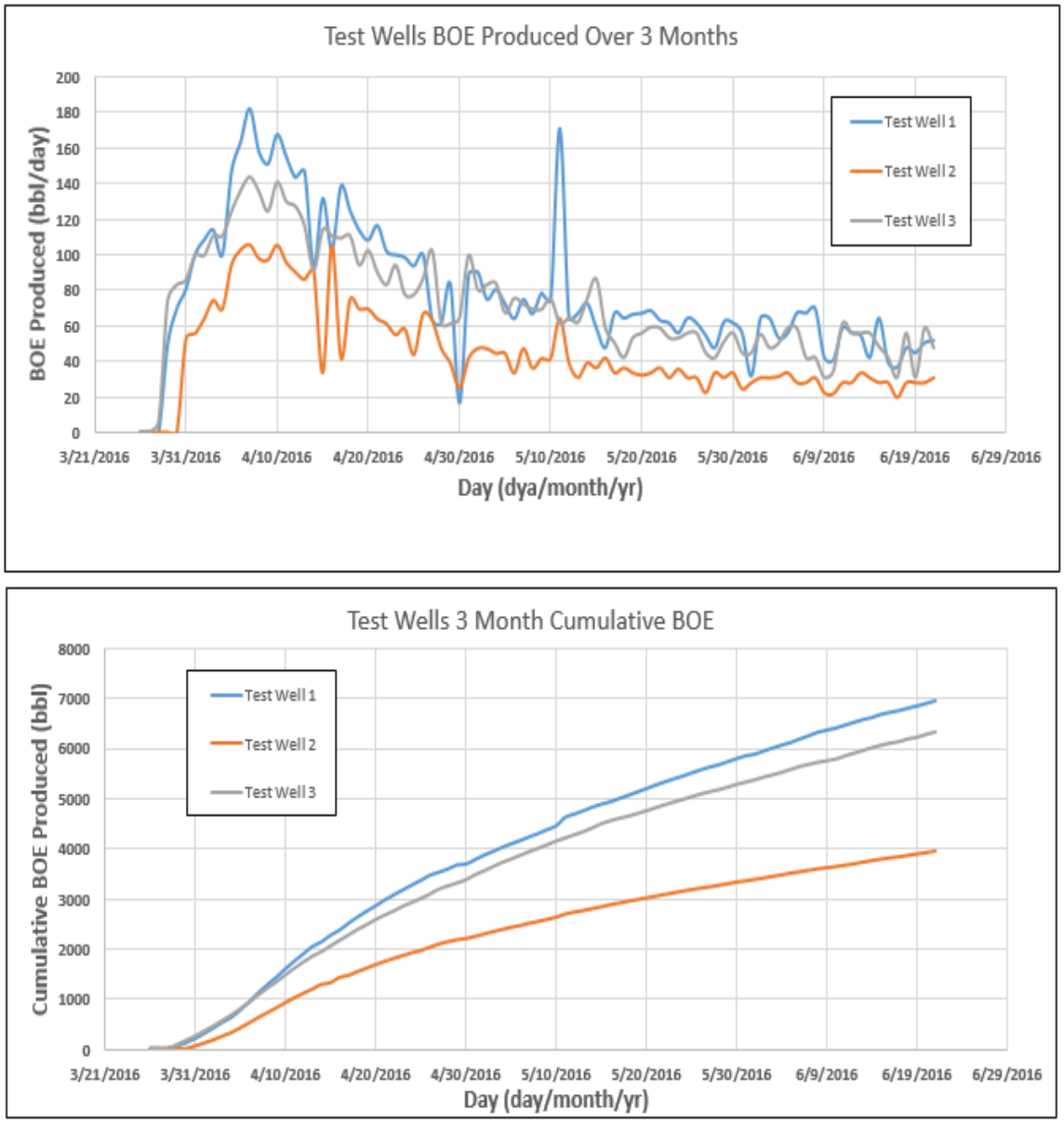

Figure 4.5. Test well three-month daily and cumulative BOE.

Table 4.1: Completions design rate parameters.

Standard Design (4 cluster 120 perforations)	Limited Entry (10 cluster 40 perforations)
100 BPM	70 BPM
------	80 BPM
------	90 BPM
------	100 BPM

Table 4.2: Final job fracture area results taken from Figure 4.2.

Standard Design (4 cluster/120 perfs)	Fracture Area (ft2)	Limited Entry (10 cluster/40 perfs)	Fracture Area (ft2)
100 BPM	627651	70 BPM	609543
------	------	80 BPM	647360
------	------	90 BPM	708863
------	------	100 BPM	752818

Table 4.3 Diverter concentration inputs.

Diverter %	Concentration (PPG)
0	0.00
50	0.25
100	0.50
200	1.00
400	2.00

Table 4.4: Fracture area growth from diverter concentration.

Diverter Concentration (PPG)	Limited Entry (10 cluster/40 perfs)	Standard Design (4 cluster/120 perfs)
-------	Fracture Area (ft2)	
0.00	557795	537505
0.25	887095	741755
0.50	881180	741755
1.00	709465	728365
2.00	753165	727625

CHAPTER 5

CONCLUSIONS AND FUTURE RECOMMENDATIONS

There are multiple factors that dictate well performance. Each choice has a significant influence on a well ranging from initial material costs and time required to complete the well to the expected ultimate recovery. There are many challenges towards accounting for the effects of natural fractures during hydraulic fracture stimulation. Natural fractures can cause unanticipated stress shadowing affects, complex fluid and proppant transport paths, and tortuous fracture paths. The demand for drilling in unconventional formations containing complex fracture systems is increasing. Potential solutions, such as limited entry design and diversion techniques, exist, but require optimization. It is important that accurate numerical solutions pertaining to diverter and completions design be incorporated into complex fracture modeling platforms that can accurately predict the outputs of real-time treatment plans.

5.1 Cluster and diverter analysis conclusions

It is concluded that the limited entry completions design for the test wells is feasible. The location of the clusters and perforations are strategically placed in stress zones that will cause higher fracture area growth and production. The limited entry test wells reported a 17% increase in fracture area. This area increase is likely due to reducing the

amount of inefficient perforations.

The use of diverter is common. However, no industry numerical modeling tool simulates the effects of diverter placement propagated natural fractures. User manipulation of the fracture sets, along with the combined use of Mangrove and FracMan, was required in developing a valid diversion solution. Simulations in this study analyzed the effects of various diverter concentrations. Final fracture area results yielded a 58% increase in fracture area growth between the clean concentration (0 PPG) and actual pump schedule concentration (0.5 PPG). There was no observable gain when increasing the concentration past a certain extent.

The key to validating the effects of diversion and limited entry is the production results. The three-month cumulative production from the limited entry well had similar BOE results compared to the standard completions design. No clear increase in performance can be due to multiple factors:

- Porosity in this reservoir is difficult to define. It is dictated by drilling penetration rate, torque on the mud motor (standpipe pressure), cuttings (percentage limestone), gas shows, and fluorescence. These are all subjectively integrated to establish pay and non-pay intervals in the lateral.
- Porosity in this reservoir is laterally very discontinuous. That is to say that even though the lateral may not encounter porosity at the same location, oil filled porosity looming 10’ away from the well bore that can be reached with a completion.

  There exist multiple degrees of freedom in the system. Each parameter affects reservoir quality and their impacts can vary greatly between each well.

However, the limited entry design still shows value. Water production from the limited entry well was 20% less over three months. These results were achieved by reducing the perforation density by two-thirds. performance may be due to the fracture network generated. Large half-length hydraulic fractures are produced when one perforation receives majority of fluid. Large half-length hydraulic fractures not only invade the drainage radius of nearby wells, but also fail to utilize the localized natural fracture network near the wellbore. Consequently, single large hydraulic fractures create three problems: the 1) production is limited and originates from limited amount of perforations, 2) water volumes are decreased in poor payzones and lead to poor natural fracture propagation, and 3) nearby wells are drained faster.

5.2 Future well design recommendations

It is recommended that perspective operating company of the test wells consider incorporating a process that accurately solves for geomechanical properties of a future planned well. The completions design of the well has a heavy impact on production performance best on the cases studied. Furthermore, a diversion modeling approach has been developed by manipulating the capabilities of FracMan and Mangrove. It is recommended that collaboration be conducted with the two parties for developing and integrating a standard diverter analysis option. The parameters simulated can be used by drilling and completions engineers to further improve field production and possibly reduce the capital costs of a well by evaluating the possibilities of: 1) using ultra high mesh diverter to access smaller width fractures, 2) strategically placing the clusters and perforations into the ideal stress zones, and 3) simulating future wells with FMI data to further calibrate the

limited entry and diverter model. More simulations under similar design criteria will ultimately help engineers select design criteria that will optimize the performance of newly drilled wells.

5.3 Thesis contributions to the scientific community

The material provided in this thesis has shown that it is possible to use Mangrove and FracMan to develop a reasonable discrete fracture network model that can simulate fracture changes under specific completions and diverter conditions. These numerical packages allow a representative rendition of in-situ natural fractures and provide a basic method for simulating injection. The modeling of the test wells serves as a benchmark for simulating more complex problems, such as fracture effects on nearby wells, lithology changes, and faults. It is important to note that variations in any of the spatially-local input values used could have led to changes in the modeled system. This project has succeeded in providing a proof-of-concept that FracMan and Mangrove can be used as a platform for understanding injection into natural fractures. It can serve as 1) a staging point towards developing other model simulations with an eventual increase in complexity, 2) a bridge in solving completions and diversion questions associated with the natural fractures and hydraulic fracture systems, and 3) be used for accurate production forecasting.

APPENDIX A

STACKED HEIGHT GROWTH EQUATION WIDTH SOLUTION

$$w(h,z) = \frac{4}{E\pi} \sum_{j=1}^{Nstack} \int_{H_{j-1}}^{H_j} \left| P_{cp,\,j} + \rho_{f,\,j} g(h_{cp,\,j} - a) - \sigma(a) \right| \times \cosh^{-1} \left[\frac{z\left(\frac{h-2a}{h}\right) + a}{|\,z-a\,|} \right] da \qquad (2.9)$$

$$= \frac{4}{E\pi} \{ I_1 - I_2 + I_3 \}$$

$$I_1 = \sum_{j=1}^{Nstack} \int_{H_{j-1}}^{H_j} \left| P_{cp,\,j} + \rho_{f,\,j} g(h_{cp,\,j} - a) - \sigma(a) \right| \times \cosh^{-1} \left[\frac{z\left(\frac{h-2a}{h}\right) + a}{|\,z-a\,|} \right] da \qquad (i)$$

$$I_1 = I_{1,1} - I_{1,2} \qquad (ii)$$

$$I_{1,1} = \sum_{j=1}^{Nstack} \int_{H_{j-1}}^{H_j} \left| P_{cp,\,j} + \rho_{f,\,j} g(h_{cp,\,j}) \right| \times \cosh^{-1} \left[\frac{z\left(\frac{h-2a}{h}\right) + a}{|\,z-a\,|} \right] da \qquad (iii)$$

$$I_{1,2} = \sum_{j=1}^{Nstack} \int_{Hj-1}^{Hj} \left|\rho_{f,j} g a\right| \times \cosh^{-1}\left[\frac{z\left(\frac{h-2a}{h}\right)+a}{|z-a|}\right] da \qquad (iv)$$

$$I_{1,1} = \sum_{j=1}^{Nstack} \left[[P_{cp,j} + \rho_{f,j} g(h_{cp,j})] \times \left\{ \begin{array}{l} (a-z)\cosh^{-1}\left|\dfrac{z\left(\frac{h-2a}{h}\right)+a}{|z-a|}\right| - \\ \sqrt{z(h-z)}\arcsin\left(\dfrac{h-2a}{h}\right) \end{array} \right\} \right]_{a=Hj-1}^{a=Hj} \qquad (v)$$

$$I_{1,2} = \sum_{j=1}^{Nstack} \rho_{f,j} g \left[\begin{array}{l} -\dfrac{a^2-z^2}{2}\cosh^{-1}\left\{\dfrac{z\left(\frac{h-2a}{h}\right)+a}{|z-a|}\right\} - \dfrac{(h+2z)\sqrt{z(h-z)}}{4} \\ \times \arcsin\left[\dfrac{h-2a}{h}\right] - \dfrac{\sqrt{az}\sqrt{(h-z)(h-a)}}{2} \end{array} \right]_{a=Hj-1}^{a=Hj} \qquad (vi)$$

$$I_2 = \int_0^h \sigma_n \cosh^{-1}\left[\frac{z\left(\frac{h-2a}{h}\right)+a}{|z-a|}\right] da \qquad (vii)$$

$$I_2 = \sigma_n \pi \sqrt{z(h-z)} \qquad (viii)$$

$$I_3 = \sum_{i=1}^{n-1} \int_0^h [\sigma_{i+1} - \sigma_i] \cosh^{-1}\left[\frac{z\left(\frac{h-2a}{h}\right)+a}{|z-a|}\right] da \qquad (ix)$$

$$I_3 = \sum_{i=1}^{n-1} [\sigma_{i+1} - \sigma_i] \cosh^{-1} \left[\frac{z\left(\frac{h-2a}{h}\right) + a}{|z-a|} \right] + \sqrt{z(h-z)} ar\cos\left(\frac{h-2h_i}{h}\right) \quad (x)$$

- σn ..... In-situ stress at the top of the fracture tip,
- σi ..... In-situ stress at the *i*-th layer

APPENDIX B

STACKED HEIGHT GROWTH EQUATION HEIGHT SOLUTION

- 2.9a. Stress Intensity factor above the fracture

$$K_{Iup} = \sqrt{\frac{2}{\pi h}} \sum_{j=1}^{Nstack} \int_{H_{j-1}}^{H_j} \left| P_{cp,\,j} + \rho_{f,\,j} g (h_{cp,\,j} - a) - \sigma(a) \right| \sqrt{\frac{a}{h-a}}\, da \qquad (2.11a)$$

$$= \sqrt{\frac{2}{\pi h}} \sum_{j=1}^{Nstack} \{ I_1 - I_2 + I_3 \}$$

$$I_1 = I_{1,1} - I_{1,2} \qquad (a.i)$$

$$I_{1,1} = \sum_{j=1}^{Nstack} \int_{H_{j-1}}^{H_j} \left[P_{cp,\,j} + \rho_{f,\,j} g h_{cp,\,j} \right] \sqrt{\frac{a}{h-a}}\, da \qquad (a.ii)$$

$$I_{1,2} = \sum_{j=1}^{Nstack} \int_{H_{j-1}}^{H_j} \left[\rho_{f,\,j} g a \right] \times \sqrt{\frac{a}{h-a}}\, da \qquad (a.iii)$$

$$I_{1,1} = \sum_{j=1}^{Nstack} \int_{Hj-1}^{Hj} \left[P_{cp,\,j} + \rho_{f,\,j} g h_{cp,\,j}\right] \left[-\sqrt{a(h-a)} + +h \arctan\sqrt{\frac{a}{h-a}} \right]_{a=Hj-1}^{a=Hj} \qquad \text{(a.}iv\text{)}$$

$$I_{1,2} = \sum_{j=1}^{Nstack} \int_{Hj-1}^{Hj} \left[\rho_{f,\,j} g\right] \left[-\frac{2a+3h}{4}\sqrt{a(h-a)} - \frac{3h^2}{8} \arcsin\left(\frac{h-2a}{h}\right) \right]_{a=Hj-1}^{a=Hj} \qquad \text{(a.}v\text{)}$$

$$I_2 = \int_0^h \sigma_n \sqrt{\frac{a}{h-a}}\, da \qquad \text{(a.}vi\text{)}$$

$$I_2 = \sigma_n \frac{\pi h}{2} \qquad \text{(a.}vii\text{)}$$

$$I_3 = \sum_{i=1}^{n-1} \int_0^h \left[\sigma_{i+1_i} - \sigma_i\right] \times \sqrt{\frac{a}{h-a}}\, da \qquad \text{(a.}viii\text{)}$$

$$I_3 = \sum_{i=1}^{n-1} \left(\sigma_{i+1_i} - \sigma_i\right) \left[\frac{h}{2} ar\cos\left(\frac{h-2h_i}{h}\right) - \sqrt{h_i(h-h_i}\right] \qquad \text{(a.}ix\text{)}$$

- 2.9b. Stress Intensity factor below the fracture

$$K_{Idown} = \sqrt{\frac{2}{\pi h}} \sum_{j=1}^{Nstack} \int_{Hj-1}^{Hj} \left|P_{cp,\,j} + \rho_{f,\,j} g(h_{cp,\,j} - a) - \sigma(a)\right| \sqrt{\frac{a}{h-a}}\, da \qquad \text{(2.11b)}$$

$$I_1 = I_{1,1} - I_{1,2} \qquad \text{(b.}i\text{)}$$

$$I_{1,1} = \sum_{j=1}^{Nstack} \int_{Hj-1}^{Hj} \left[P_{cp,\,j} + \rho_{f\,,\,j} g h_{cp,\,j}\right] \sqrt{\frac{h-a}{a}}\, da \qquad \text{(b.}ii\text{)}$$

$$I_{1,2} = \sum_{j=1}^{Nstack} \int_{Hj-1}^{Hj} \left|\rho_{f\,,\,j} g a\right| \times \sqrt{\frac{h-a}{a}}\, da \qquad \text{(b.}iii\text{)}$$

$$I_{1,1} = \sum_{j=1}^{Nstack} \int_{Hj-1}^{Hj} \left[P_{cp,\,j} + \rho_{f\,,\,j} g h_{cp,\,j}\right] \left[\sqrt{a(h-a)} + + h \arctan \sqrt{\frac{a}{h-a}} \right]_{a=Hj-1}^{a=Hj} \qquad \text{(b.}iv\text{)}$$

$$I_{1,2} = \sum_{j=1}^{Nstack} \int_{Hj-1}^{Hj} \left|\rho_{f\,,\,j} g\right| \left[\frac{2a-h}{4} \sqrt{a(h-a)} - \frac{h^2}{8} \arcsin\left(\frac{h-2a}{h}\right) \right]_{a=Hj-1}^{a=Hj} \qquad \text{(b.}v\text{)}$$

$$I_2 = \int_0^h \sigma_n \sqrt{\frac{h-a}{a}\, da} \qquad \text{(b.}vi\text{)}$$

$$I_2 = \sigma_n \frac{\pi h}{2} \qquad \text{(b.}vii\text{)}$$

$$I_3 = \sum_{i=1}^{n-1} \int_0^h \left[\sigma_{i+1_i} - \sigma_i\right] \times \sqrt{\frac{h-a}{a}}\, da \qquad \text{(b.v}iii\text{)}$$

$$I_3 = \sum_{i=1}^{n-1} \left(\sigma_{i+1_i} - \sigma_i\right) \left[\frac{h}{2} ar\cos\left(\frac{h-2h_i}{h}\right) - \sqrt{h_i(h-h_i}\right] \qquad \text{(b.}ix\text{)}$$

REFERENCES

[1] Barree, R. D. Economic Optimization of Horizontal-Well Completions in Unconventional Reservoirs. Society of Petroleum Engineers SPE 168612, 2015.

[2] Wan, Jihn. Coupled Well and Reservoir Simulation Models to Optimize Completions Design and Operations for Subsurface Control. Society of Petroleum Engineers SPE 113635, 9 June 2008.

[3] Cohen, Charles E. Parametric Study on Completion Design in Shale Reservoirs Based on Fracturing-to-Production Simulations. International Petroleum Technology Conference IPTC 17462, 2014.

[4] Weng, Xiaowei. Modeling of Hydraulic-Fracture-Network Propagation in a Naturally Fractured Formation. Society of Petroleum Engineers SPE 140253, Nov. 2011.

[5] Kreese, O., C. Cohen, and X. Weng. Numerical Modeling of Hydraulic Fracturing in Naturally Fractured Formations. American Rock Mechanics Association 11-363, 2011.

[6] Cravero, M., and S. Ponti. D Simulation and Aggregation of Fracture Network. American Rock Mechanics Association 07-019, May 2007.

[7] Mullen, J., Lowry, J.C., and Nwabuoku, K.C. 2010. Lessons Learned Developing the Eagle Ford Shale. Paper SPE 138446 presented at the SPE Tight Gas Conference, San Antonio, Texas, 2–3 November. http://dx.doi.org/10.2118/138446-MS.

[8] Cipolla, C., Mack, M., and Maxwell, S. 2010b. Reducing Exploration and Appraisal Risk in Low Permeability Reservoirs Using Microseismic Fracture Mapping - Part 2. SPE 138103 presented at the SPE Latin American & Caribbean Petroleum Engineering Conference held in Lima, Peru, 1–3 December 2010

[9] Shin, D. and Sharma, M. 2014. Factors Controlling the Simultaneous Propagation of Multiple Competing Fractures in a Horizontal Well. Paper SPE 168599 presented at the SPE Hydraulic Fracturing Technology Conference, The Woodlands, Texas, 4–6 February. http://dx.doi.org/10.2118/168599-MS.

[10] Cheng, Y. 2012. Mechanical Interaction of Multiple Fractures—Exploring Impacts of the Selection of the Spacing/Number of Perforation Clusters on Horizontal Shale Gas Wells. *SPE J.* 17 (4): 992–1001. Paper SPE 125769-PA.

[11] Walker K., Wutherich K. and Terry J. Engineered Perforation design improves Fracture Placement and Productivity in Horizontal Shale Gas Wells. Paper SPE 154582 presented at the SPE Americas Unconventional Resources Conference, 5-7 June 2012, Pittsburg, Pennsylvania, USA

[12] Cipolla C., Weng X, Malpani, R., and Luo, F. 2010 Shale Gas Production Decline Trend Over Time and Basins. Paper SPE 135555 presented at SPE Annual Technical Conference and Exhibition, Florence, Italy, 19-22 September.

[13] Ahmed, M., and Andrea Nino-Penaloza. Engineering Solid Particulate Diverter to Control Fracture Complexity: Experimental Study. Society of Petroleum Engineers SPE 179144-MS, May 2016.

[14]. Allison, D., Curry, S., and Todd, B. 2011. Restimulation of Wells using Biodegradable Particulates as Temporary Diverting Agents. Paper CSUG/SPE 149221 presented at the Canadian Unconventional Resources Converence, Calgary, Alberta, Canada, 15-17 November. Dio: 10.2118/149221-MS

[15] Fisher, M.L., B.M. Davidson, A.K. Goodwin, E.O. Fielder, W.S. Buckler, and N.P. Steinberger. 2002. Integrating Fracture Mapping Technologies to Optimize Stimulations in the Barnett Shale. Paper SPE 77441 presented at the 2002 SPE Annual Technical Conference and Exhibition, San Antonio, Texas, USA, September 29-October 2.

[16] Daniels, J., G. Walters, J. Le Calvez, J. Lassek, and D. Bentley. 2007. Contacting More of the Barnett Shale Through an Integration of Real-Time Microseismic Monitoring, Petrophysics, and Hydraulic Fracture Design. Paper SPE 110562 presented at the 2007 SPE Annual Technical Conference and Exhibition, Anaheim, California, USA, October 12-14.

[17] Xu, W., J.L. Calvez, and M. Thiercelin. 2009. Characterization of Hydraulically-Induced Fracture Network Using Treatment and Microseismic Data in a Tight-Gas Formation: A Goemechanical Approach, Paper SPE 125237 presented at the 2009 SPE Tight Gas Completions Conference, San Antonio, Texas, USA, 15-17 June.

[18] Meyer, B.R. and L.W. Bazan. 2011. A Discrete Fracture Network Model for Hydraulically-Induced Fractures: Theory, Parametric and Case Studies, Paper SPE 140514 presented at the SPE Hydraulic Fracturing Conference and Exhibition, Woodlands, Texas, January 24-26.

[19]Kresse, O., C. Cohen, and X. Weng. Numerical Modeling of Hydraulic Fracturing in Naturally Fractured Formations. American Rock Mechanics Association ARMA 11-363, 26-29 June 2011.

[20] Renshaw, C.E. and D.D. Pollard. 1995. An Experimentally Verified Criterion for Propagation Across Unbounded Frictional Interfaces in Brittle, Linear Elastic Materials. *Int. J. Rock Mech. Min. Sci. & Geomech. Abstre.,* 32: 237-249

[21] Perkins, T.K. and Kern, L.R. 1961. Widths of Hydraulic Fractures. J Pet Technol 13 (9): 937–949. SPE-89-PA. http://dx.doi.org/10.2118/89-PA.

[22]. Mack, M.G. and N.R. Warpinski. 2000. Mechanics of Hydraulic Fracturing. Chapter 6, *Reservori Stimulation,* 3rd Ed. Eds. Economides, M.J. and Nolte, K.G. John Wiley & Sons.

[23]. Gu, H., and X. Weng. Hydraulic Fracture Crossing Natural Fracture at Non-Orthogonal Angles, A Criterion, Its Validation and Applications. Society of Petroleum Engineers SPE 139984, 24 Jan. 2011.

[24]. Jaeger, J.C., Cook, N.G.W., and Zimmerman, R.w. (2007) Fundamentals of Rock Mechanics, 4th ed., Blackwell Publishing, Malden, MA, U.S.A.

[25]. Weng, X., Kresse, O., Cohen, C., and Wu, R., and Gu, H. (2011) Modeling of Hydraulic Fracture Network Propagation in a Naturally Fractured Formation, paper SPE 140253, to be presented at the SPE Hydraulic Fracturing Technology Conference, The Woodlands, Texas, Jan. 24-26.

[26]. Crouch, S.L. and A.<. Starfield. 1983. Boundary Element Methods in Solif Mechanics, George Allen & Unwin Ltd, London.

[27]. Olson, J.E. 2004. Predicting Fracture Swarms – the Influence of Subcritical Crack Growth and the Crack-Tip Process Zone on Joint Spacing in Rock. In The initiation, Propagation, and Arrest of Joints and Other Fractures, Geological Society of London Special Publication 231, eds. J.W. Cosgrove and T. Engelder:73-87.

[28]. Daneshy, A. 1978. Numerical Solution of Sand Transport in Hydraulic Fracturing. J. Pet. Tech., January 1978 (SPE 5636): 132-140.

[29]. Hossain, M. E., and A. A. Al-Mejed. Fundamentals of Sustainable Drilling E ngineering. Vol. 1. Hoboken: John Wiley & Sons, 2015.

[30]. J. McLennan, R. Carden, D. Curry, and C. Stone. *Underbalanced Drilling Manual*. Chicago: Gas Research Institute, n.d. Print. GRI Reference No. GRI-97/0236.

[31]. Economides, M., and K. Nolte. *Reservoir Stimulation*. Hoboken: John Wiley & Sons, 2000.

[32]. Crain, E. R. Elastic Constants/Mechanical Properties. Crain's Petrophysical Handbook, 1978-2016.